**Title:**

# Nuclear translocation of LINE-1 encoded ORF1p alters nuclear envelope integrity and disrupts nucleocytoplasmic transport in human neurons

**Authors:**

Rania Znaidi[1], Olivia Massiani-Beaudoin[1], Philippe Mailly[2], Héloïse Monnet[2], The Brainbank Neuro- CEB Neuropathology Network[3], Rajiv L. Joshi[1]* and Julia Fuchs[1]*

**Affiliations:**

[1]CIRB, Collège de France, Université PSL, CNRS, INSERM, 75005 Paris, France,

[2]Orion Imaging Facility, CIRB, Collège de France, Université PSL, CNRS, INSERM, Labex Memolife, 75005 Paris, France,

[3]The Neuro-CEB Neuropathology network includes: Franck Letournel (CHU Angers), Marie-Laure Martin-Négrier (CHU Bordeaux), Maxime Faisant (CHU Caen), Catherine Godfraind (CHU Clermont-Ferrand), Claude-Alain Maurage (CHU Lille), Vincent Deramecourt (CHU Lille), Mathilde Duchesne (CHU Limoges), David Meyronnet (CHU Lyon), Clémence Delteil (CHU Marseille), Valérie Rigau (CHU Montpellier), Danielle Seilhean (CHU PS, Paris), Susana Boluda (CHU PS, Paris), Isabelle Plu (CHU PS, Paris), Dan Christian Chiforeanu (CHU Rennes), Florent Marguet (CHU Rouen), Béatrice Lannes (CHU Strasbourg).

***For correspondence:**

J.F. (Julia.fuchs@college-de-france.fr); R.L.J. (rajiv.joshi@college-de-france.fr)

**Key words:** Retrotransposons; LINE-1 ; ORF1p ; nuclear envelope ; nuclear pore complex ; nucleocytoplasmic transport ; neurodegeneration.

**Abstract**

LINE-1 retrotransposons are emerging as possible culprits in neurodegenerative diseases. However, the molecular mechanisms underlying the pathogenic role of LINE-1 and their encoded proteins ORF1p and ORF2p are still not completely understood. While the endonuclease and reverse transcriptase activities of ORF2p have been associated with DNA damage and inflammation, no pathogenic role has yet been assigned to ORF1p. Using a neuronal model of oxidative stress displaying increased LINE-1 expression, we report here that ORF1p stress-dependently translocated into the nucleus, localized to the nuclear envelope and directly interacted with nuclear import proteins, nuclear pore complex components and the inner nuclear lamina. Stress-dependent targeting of nuclear envelope components by ORF1p altered nuclear envelope integrity, disrupted nucleocytoplasmic transport and induced heterochromatin destructuration, features associated with neurodegenerative diseases and aging. Neurons of post-mortem Parkinson disease (PD) patients and non-PD affected controls expressed ORF1p and nuclear ORF1p levels correlated with altered nuclear shape in PD. Overexpression of ORF1p in neurons in the absence of stress recapitulated nuclear envelope dysfunctions and increased nuclear ORF1p levels correlated with a loss of nuclear circularity. Stress-induced nuclear alterations were restored by blocking ORF1p nuclear import or by the small molecule remodelin. This study thus reveals a retrotransposition- and ORF2p-independent pathogenic action of ORF1p at the nuclear envelope and points to ORF1p as a novel target for neuroprotection.

## Introduction

Repetitive sequences derived from transposable elements (TEs) represent 45% of the human genome, including LTR (Long Terminal Repeat) and non-LTR retroelements. Non-LTR retrotransposons of the Long Interspersed Element-1 (LINE-1) family have been the most active TEs in mammalian genomes and LINE-1-derived sequences represent almost 21% of the human genome which carries nearly 500000 LINE-1 copies [1]. Although most of these LINE-1 copies are remnants of past retrotransposition events and are truncated or mutated, the reference human genome still carries 146 full-length LINE-1 copies (according to LINE-1Base database) which can be autonomously active and competent for retrotransposition [2]. The full-length LINE-1 sense strand codes for two proteins, namely ORF1p and ORF2p, which are required for retrotransposition. ORF1p is an RNA binding protein and ORF2p encompasses reverse transcriptase and endonuclease activities. Since LINE-1 activation can lead to deleterious consequences such as DNA damage and genomic instability [3–6], senescence and inflammation [7,8], these TEs are repressed in most somatic cells at the transcriptional and post-transcriptional level. Failure of these repressive mechanisms can lead to the activation of LINE-1 and other TEs in the context of aging or human diseases like cancer.

Several recent studies have reported that TE activation might be linked to neurodegenerative diseases (NDs) such as Alzheimer's disease (AD), non-AD tauopathies, Parkinson disease (PD), Amyotrophic Lateral Sclerosis (ALS) and Huntington disease (HD) [5,9–14]. Although NDs present many common hallmarks such as pathological protein aggregation, synaptic and neuronal network dysfunction, aberrant proteostasis, cytoskeletal abnormalities, altered energy homeostasis, DNA and RNA defects, inflammation, oxidative stress and neuronal cell death [15,16], the genetic basis and the molecular and cellular

101 mechanisms underlying neurodegeneration still remain elusive. In this regard, recent work
102 from our group [5,17] and others [13,14,18] suggests that TE activation could directly contribute to
103 neuronal dysfunctions associated with NDs. Indeed, several pathogenic features of NDs might
104 actually be linked to TE de-repression [19,20]. While the deleterious consequences attributed to
105 the endonuclease and reverse transcriptase activities of LINE-1 ORF2p (i.e. DNA strand
106 breaks, cytosolic single-stranded DNA inducing innate immune activation and inflammation)
107 are beginning to be well unraveled, no particular pathogenic function has yet been assigned to
108 the RNA chaperone ORF1p.

109 To directly address the consequences of endogenous full-length LINE-1 activation and
110 increased LINE-1-encoded proteins in adult neurons, we used a neuronal model of acute
111 oxidative stress displaying an increase in LINE-1 encoded ORF1p expression. Using this
112 model, we uncovered a so far unrecognized pathogenic role of ORF1p in potentiating nuclear
113 envelope (NE) barrier alterations. This suggests that stressed neurons are susceptible to
114 ORF1p mediated NE perturbations leading to the amplification of NE dysfunctions which are
115 a novel emerging feature of many NDs.

116

117 **Materiel and methods**

118

119 **Cell culture**

120 The Lund Human Mesencephalic (LUHMES) cell line is a conditionally immortalized cell
121 line. These cells are derived from the tetracycline-controlled, v-myc-overexpressing human
122 mesencephalic cell line MESC2.10 [21,22]. The culturing and handling procedure of LUHMES
123 cells were as described previously [21]. LUHMES cells can be differentiated into mature
124 dopaminergic neurons. The differentiation was performed following the two-step protocol
125 previously established [23]. Cell culture flasks, multi well plates and glass coverslips used for

126 LUHMES culture were pre-coated by adding 50 µg/ml poly-L-ornithine (Sigma) diluted in
127 1X PBS (Phosphate buffered saline) for 1 h at 37°C, washed 3 times in 1X PBS, and then
128 incubated with 1 µg/ml fibronectin (Sigma) diluted in 1X PBS for 3 h minimum at 37°C to
129 promote cell attachment. Uncapped flasks were air-dried before cell plating.

130 The base cell culture medium consisted of Advanced DMEM/F12 (ThermoFisher
131 Scientific), N2-Supplement (ThermoFisher Scientific) and 2 mM GlutaMAX (ThermoFisher
132 Scientific, 35050061) which was supplemented by 40 ng/ml recombinant human basic
133 fibroblast growth factor FGF (Peprotech) during proliferation, at 37°C in 100% humidified air
134 with 5% CO2 until 70%–80% of cellular confluence is reached.

135 The differentiation process was initiated by the shut-down of v-myc by adding 1
136 µg/ml doxycycline (Sigma) in the base medium supplemented with 2 ng/ml recombinant
137 human glial-derived neurotrophic factor GDNF (Peprotech) and 1 mM cAMP (Sigma). The
138 pre-differentiated neurons were replated 48 h later at a defined density of 150 000 cells/well
139 in 24-well plates or $10^6$ cells/well in 6-well plates. To confirm successful generation of post-
140 mitotic LUHMES, expression of neuronal and dopaminergic markers was assessed
141 throughout the differentiation protocol, which lasts a total of 5 days (Fig. 1A; Suppl. Fig. 1A).
142 All experiments were performed on day 5 of differentiation, at which point LUHMES cells
143 were considered to be completely mature post-mitotic neurons.

144

145 **Arsenite-induced oxidative stress**

146 Stock of sodium arsenite solution ($NaAsO_2$) (Sigma) was stored at room temperature.
147 Dilutions were carried out shortly before each experiment. Fully differentiated LUHMES
148 cells (at day 5 of differentiation) were subjected to arsenite during 1 h at 37°C at a
149 concentration of 50 µM to induce oxidative stress.

150

151

152 **Drug treatment**

153 For treatment with remodelin (a gift from Drs. R. Rodriguez and L. Colombeau),
154 differentiated neurons at day 4 of differentiation, were incubated in fresh culture medium
155 containing remodelin (10 μM) or DMSO for 24 h and then subjected to oxidative stress using
156 arsenite (50 μM) for 1 h (in the presence of remodelin). For stavudine treatment,
157 differentiated neurons at day 4 of differentiation, were incubated in fresh culture medium
158 containing stavudine (10 μM) or NaCl for 24 h, and then subjected to oxidative stress using
159 arsenite (50 μM) for 1 h (in the presence of stavudine). For treatment using nuclear import
160 inhibitors, differentiated neurons at day 5 of differentiation, were incubated in fresh culture
161 medium containing ivermectin (5 μM; CliniSciences) and importazole (10 μM; Scientific
162 Laboratory Supplies) or DMSO for 2 h, and were then treated with arsenite (50 μM) for 1 h.
163 In all cases, neurons were then fixed and processed for immunocytochemistry.

164

165 **Transfection methods**

166 Adherent electroporation (Nucleofection): LUHMES cells were seeded at a density of 150
167 000 cells/well into 24-well plates already containing cover-slips pre-coated with poly-L-
168 ornithine and fibronectine and were differentiated as described in Cell culture section. After 3
169 days of differentiation, cell culture medium was replaced by pre-warmed fresh medium and
170 incubated for 1 h at 37°C prior to transfection. LUHMES cells were transfected by
171 Nucleofection using the AMAXA 4D-Nucleofector® Y Unit (Lonza) which enables the direct
172 Nucleofection (by electroporation) of cells in adherence in 24-well culture plates using the
173 AD1 4D-Nucleofector™ Y Kit (Lonza, V4YP-1A24) for neuronal cells electroporation. The
174 ER-100 program was the most appropriate to LUHMES cells in terms of transfection
175 efficiency and viability and was used for all subsequent transfections. One Nucleofection

176 sample contained 150 000 cells/well, 10 µg plasmid DNA (pcDNA3-ORF1-HA, expressing
177 ORF1p with an N-Ter HA tag; a gift from Dr. J. Moran and Dr. Y. Ariumi) or 10 µg
178 pmaxGFP vector and 350 µl AD1 4D-Nucleofector Y solution. The 24-well dipping electrode
179 array (provided in the kit) was inserted into the plate and cells were transfected by using the
180 ER-100 Nucleofector program. After nucleofection, AD1 solution was removed and the cells
181 were immediately washed once with fresh medium and incubated in humidified 37°C / 5%
182 CO2 incubator. Media was not changed until analysis at day 5 of differentiation (48 h after
183 transfection). Transfection efficiency (48 h after transfection) was monitored by fluorescence
184 microscopy.
185
186 **Protein extraction**
187 After aspirating media, cells were washed one time with 1X PBS. 200 to 500 µl of 1X RIPA
188 lysis buffer (50 mM Tris-HCL pH 8, 150 mM Nacl, 0,5% Sodium deoxycholate, 1% NP-40,
189 0,1% SDS) with 1X protease inhibitor (Sigma) was added to each well in the plate. Cells were
190 scraped and lysates were transferred to a sterile microtube. The lysates were incubated on ice
191 for 30 min and sonicated using the Bioruptor UCD-200 for 15 min (30s on/30s off) on ice at
192 high power to shear contaminating DNA. After collecting the supernatant (avoiding the
193 pellet) into new microtubes, protein concentration was determined using Pierce™ BCA
194 Protein Assay Kit. Aliquot of lysates were stored at -20ºC avoiding multiple freeze/thaw
195 cycles. Proteins were taken in 1X Laemmli buffer (250 mM Tris pH 6,8, 10% sodium dodecyl
196 sulfate, 1,25% bromophenol blue, 5% β-mercaptoethanol, 50% glycerol) containing DTT,
197 boiled 10 minutes at 95°C and stored at -20°C until analyzed.
198
199 **Western blot analysis**
200 A 1.5 mm NuPAGE 4-12% Bis-Tris-Gel (Invitrogen™) polyacrylamide gel was used for

201 Western blots. 10 µg of protein were loaded per well. Gel migrated in NuPAGE™ MES SDS
202 running buffer (1X) (Invitrogen™) for 55 minutes at 200 V. Gels were transferred into a
203 methanol activated PVDF membrane (Immobilon) in a transfer buffer (Tris 25 mM, pH 8,3
204 and glycine 192 mM) during 1 h at 400 mA at 4°C. For blocking, 5% milk in TBST (0,2%
205 Tween 20, 150 mM NaCI, 10 mM Tris pH:8) was used during 1 h at room temperature. The
206 membranes were then incubated overnight with primary antibody anti-ORF1p 1:500 (Abcam,
207 ab245249). The membranes were incubated with anti-actin peroxidase antibody 1:20000
208 (Sigma) diluted in 5% milk in TBST, 1 h at room temperature on a shaker. The membranes
209 were washed in TBST (1X) and incubated with secondary antibody including anti-rabbit HRP
210 1:2000 (Cell Signaling) and anti-mouse HRP 1:2000 (Cell Signaling) for 1 h at room
211 temperature. After washing in TBST (1X), membranes were revealed using Clarity Western
212 ECL Substrate (Bio Rad) or Maxi Clarity Western ECL Substrate (BioRad) in a LAS-4000
213 Fujifilm system. Analysis of immunoblotting images was performed manually using Fiji
214 software.
215
216 **Immunoprecipitation**
217 For immunoprecipitation (IP) we used ORF1p (Millipore, MABC 1152) and IgG mouse
218 (Thermofisher) antibodies. The antibodies were coupled to magnetic beads using the
219 Dynabeads® Antibody Coupling Kit (Invitogen) according to the manufacturer's
220 recommendations. We used 8 µg of antibody for 1 mg of beads. The appropriate volume of
221 buffer was added to the coupled beads to achieve a final concentration of 10 mg/ml.
222 LUHMES cells were plated at a density of $20x10^6$ cells in 2 T75 flasks and grown in
223 differentiation medium for 5 days. One flask was treated with 50 µM arsenite for 1 h. Control
224 and treated cells were washed with 1X PBS and harvested using 1 ml of lysis buffer (10 mM

225 Tris HCl pH 8, 150 mM NaCl, NP40 0.5% v/v, protease inhibitor 10 µl/ml) per T75 flask.
226 Samples were sonicated for 15 min at 4°C, then centrifuged at 1200 rpm for 15 min at 4°C.
227 The supernatants obtained were transferred to a new microcentrifuge tube and then separated
228 into 3 tubes. One tube containing 50 µl of supernatant (1/10th of the test samples) was stored
229 at 4°C until the samples were analyzed. The other two tubes containing 445 µl of the
230 remaining supernatants were used for IP. Mouse IgG beads (75 µl) were added to one tube
231 and ORF1p antibody beads (75 µl) to the other tube. Each of these two tubes was then diluted
232 to 1.5 ml with buffer (10 mM Tris HCl pH8, 150 mM NaCl, 10 µl/ml protease inhibitor) to
233 dilute the NP40. The samples were then incubated overnight on a wheel at 4°C. Samples were
234 then washed 3 times with 1 ml buffer (10 mM Tris HCl pH 8, 150 mM NaCl, 10 µl/ml
235 protease inhibitor) using a magnet and then resuspended in 50 µl of the same buffer. The
236 samples were boiled in Laemmli buffer (95°C, 10 min) and 20 µl of each sample were
237 deposited on a 4-12% Nupage gel (Invitrogen). Migration was carried out in MES SDS
238 running buffer (Invitrogen) for 45 min at 200 V. The gel was then transferred onto a PVDF
239 membrane activated with methanol (Immobilon, Sigma) in glycine buffer (25 mM Tris, 200
240 mM glycine pH 8,3) for 1 h at 400 mA. The membranes were revealed using the primary
241 antibodies anti-ORF1p rabbit 1:500 (Abcam, ab245249), anti-Lamin B1 rabbit 1:1000
242 (Abcam, ab16048), the secondary anti-rabbit HRP 1:2000 (Ozyme) with the Maxi Clarity
243 Western ECL Substrate kit (BioRad). Analysis of immunoblotting images was performed
244 manually using Fiji software.
245
246 **RT-qPCR**
247 Total RNA from $5x10^5$ lysed cells was extracted using RNeasy Plus Micro Kit (Qiagen)
248 according to the manufacturer's instructions. The removal of contaminating genomic DNA
249 (gDNA) was assessed by using the ezDNase kit (Invitrogen™). After gDNA elimination,

250 RNA (300 ng) was reverse transcribed using the All-In-One 5X RT MasterMix kit (Abcam)
251 for first-strand cDNA synthesis ready for immediate real-time PCR analysis.
252 Quantitative PCR reactions were carried out in duplicates with SsoAdvanced
253 Universal SYBR® Green Supermix (Biorad) on a CFX Opus 384 (Bio-Rad,) with the
254 following program: enzyme activation at 95°C 2 min, primer denaturation at 95°C, annealing
255 at 57°C and primer extension at 72°C for 42 cycles. The following primers were used: HPRT
256 (F: CAGCCCTGGCGTCGTGATTAGT; R: CCAGCAGGTCAGCAAAGA AT); TBP (F:
257 CAGCATCACTGTTTCTTGGCGT; R: AGATAGGGATTCCGGGAGTCAT) ; LINE-1
258 5'UTR (F: GTACCGGGTTCATCTCACTAGG R: TGTGGGATATAGTCTCGTG GTG),
259 ORF1 (F: AGGAAATACAGAGAACGCCACAA) R: GCTGGATATGAAATTCTG
260 GGTTGA), LINE-1 ORF2 (F: AAATGGTGCTGGGAAAACTG ; R: GCCATTGCTTTTGG
261 TGTTTT ), 3'UTR (F : GGGAATTGAACAATGAGATCAC; R: TATACATGTGCCATGC
262 TGGTG). Data were analyzed using the ddCt method and values normalized to hypoxanthine-
263 guanine phosphoribosyl transferase (HPRT) or to glyceraldehyde-3-phosphate dehydrogenase
264 (TBP) TATA-binding protein.
265
266 **Proximity Ligation Assay (PLA)**
267 The detection of the interactions between ORF1p and Lamin B1, NUP153 and KPNB1 were
268 analyzed using proximity ligation Assay (PLA) method using Duolink® In Situ Red Starter
269 Kit Mouse/Rabbit (Sigma, DUO92101). Cells were treated according to the manufacturer's
270 instructions. After PLA, cells are mounted with a Fluoromount (Invitrogen™, 15586276).
271 Fluorescence images were acquired using a Spinning Disk W1 Yokogawa imaging system.
272 The quantification was again conducted with the custom-written plugin
273 (https://github.com/orion-cirb/Nuclei_ORF1P) described previously. In short, nuclei and
274 cytoplasms are segmented in 3D using Cellpose. Within each cell, PLA foci are detected

275 using Stardist 2D on each slice of the cell mask and then reconstructed in 3D. The foci
276 parameters are ultimately computed in each cellular compartment (cytoplasm, nucleus, outer
277 and inner nuclear membranes, and nucleoplasm).
278
279 **Immunofluorescence**
280 Immunostaining experiments on cells were assessed at 1 h after arsenite treatment. Stressed
281 and control differentiated LUHMES cells cultured in 24-well plates (150 000 cells/well) were
282 fixed with 4% paraformaldehyde (PFA) in PBS for 20 min. Immunofluorescence were
283 performed overnight at 4°C after a 20 min permeabilization in 0,2% Triton X100 in PBS and
284 incubation in blocking buffer (10 % Normal goat serum (NGS), 0,1% Triton X-100 in PBS)
285 for 1 h with the following antibodies: ORF1p 1:500 (Millipore, MABC1152 clone 4H1), TH
286 1:500 (Millipore, AB9702), Tuj1 1:1000 (Abcam, ab18207), Lamin B1 1:1000 (Abcam,
287 ab16048), KPNB1 1:500 (GTX, 133733), NUP153 1:1000 (Novus biological, NB100-93329),
288 H4K20me3 1:1000 (Abcam, ab9053), HP1 1:1000 (Cell Signaling, #2623S), TDP-43 1:600
289 (Proteintech, 107-82-2AP), HA 1:1000 (Roche, 11867423001), RanGAP1 1:500 (Santa Cruz,
290 sc-28322), γH2AX 1:1000 (Abcam, ab2893), ssDNA 1:500 (ENZO, (F7-26) ALX 804-192)
291 diluted in the blocking buffer, overnight at 4°C. For ssDNA immunostaining, cells were fixed
292 with PFA, followed by 24 h methanol incubation at -20°C, then incubated at 37°C for 4 h
293 with RNaseA. Fluorescence secondary antibodies: Alexa Fluor 555, Alexa Fluor 488, Alexa
294 Fluor 647, 1:2000 (ThermoFisher Scientific) were added for 1 h at room temperature. Nuclei
295 were stained with Hoechst 1:2000 (Invitrogen, H3570). We used Fluoromount (Invitrogen™,
296 15586276). Cells were imaged by Spinning Disk W1 Yokogawa and STED (stimulated-
297 emission-depletion) Abberior Facility line imaging systems.
298 For immunostaining of post-mortem human brain tissues, sections were fixed with 4%
299 paraformaldehyde (PFA) for 10 min. Sections were permeabilized in 0,5% Triton X-100 in

300 PBS for 20 min and incubated at 100°C for 20 min in citrate buffer (10 mM citrate buffer pH
301 6.0, 0.05% Tween 20). After blocking for 1h (10 % Normal goat serum (NGS), 0,1% Triton
302 X-100, in PBS), tissues were incubated overnight at 4°C with the following primary
303 antibodies: ORF1p 1:500 (Millipore, MABC1152 clone 4H1), Lamin A/C 1:800 (Abcam,
304 ab108595), NeuN 1:1000 (GENTEX, GTX00837) diluted in blocking buffer. The following
305 secondary antibodies were added for 1 h at room temperature: Alexa Fluor 555, Alexa Fluor
306 488, Alexa Fluor 647 1:2000 (ThermoFisher Scientific). Nuclei were stained with Hoechst
307 1:2000 (Invitrogen, H3570). Sections were treated with TrueBlack lipofuscin
308 autofluorescence quencher (OZYME, BTM23014) diluted in PBS for 10 min in the absence
309 of light. The slides were rinsed 3 × 10 min in PBS to remove excess quencher and mounted
310 with Fluoromount (Invitrogen™, 15586276). Sections were imaged by Spinning Disk W1
311 Yokogawa imaging system.
312
313 **Quantification and image analysis**
314 The quantification of ORF1p fluorescence was performed with a custom-written plugin
315 (https://github.com/orion-cirb/Nuclei_ORF1P) developed for the Fiji software [24], using Bio-
316 Formats [25] and 3D Image Suite [26] libraries. Hoechst channel is downscaled by a factor 2,
317 before detecting nuclei with the 2D-stitched version of Cellpose [27] (model = 'cyto2', diameter
318 = 100, flow threshold = 0.4, cell probability threshold = 0.0, stitching threshold = 0.5).
319 Segmented image is rescaled to original size and obtained 3D nuclei are filtered by volume to
320 avoid false positive detections. Cells in ORF1p channel are detected in the same manner as
321 nuclei. Then, each cell is associated with a nucleus having at least half of its volume in
322 contact with it. Cells without any associated nucleus are filtered out. For each cell, ORF1p
323 signal is analyzed in the following cellular compartments: cytoplasm, nucleus, outer and inner
324 nuclear membranes and nucleoplasm (Fig. 2C, E). Compartmentalization is obtained using

325 combinations of morphological operations (dilation, erosion and subtraction) of the cell and
326 nucleus masks.

327 In each compartment, the integrated intensity of ORF1p is measured and normalized
328 to ensure comparability across images. Normalization is done by subtracting the image
329 background noise, estimated as the median intensity value of the minimum intensity Z-
330 projection of the ORF1p channel. ORF1p foci are detected with Stardist 2D [28], applying a
331 model trained on a dataset of 1950 images of foci. The following settings are used: percentile
332 normalization = [0.2 - 99.8], probability threshold = 0.2, overlap threshold = 0.25. ORF1p
333 foci are then labeled in 3D and filtered by volume. The number of foci, their volume and their
334 normalized integrated intensity are computed in each cellular compartment. Results are
335 provided as an Excel file.

336 To quantify nuclear deformation, another custom plugin (https://github.com/orion-
337 cirb/HA_ORF1P_Prot/) was developed for the Fiji software, that uses the same libraries listed
338 above, CLIJ [29] and Find Focused Slices (https://sites.google.com/site/qingzongtseng/find-
339 focus?authuser=0). In brief, best focussed slice in the stack is selected. Nuclei are detected on
340 this slice with Cellpose 2D (model = 'cyto2', diameter = 120, flow threshold = 0.4, cell
341 probability threshold = 0.0), filtered by area and their circularity is computed. For each
342 nucleus, ORF1p integrated intensity is analyzed in the following compartments: nucleus,
343 outer and inner nuclear membranes and nucleoplasm. Compartments are obtained with the
344 same combinations of morphological operations than previously described.

345 In case a HA-ORF1p channel is provided, cells are detected on the best focused slice
346 with Cellpose 2D (model = 'cyto2', diameter = 200, flow threshold = 0.4, cell probability
347 threshold = 0.0) and filtered by area. Nuclei having at least one pixel in contact with a HA-
348 ORF1p cell are considered as HA-ORF1p+, other nuclei as HA-ORF1p-. The quantification
349 of the intensity of other markers than ORF1p was also performed with this plugin.

350 The analysis of human sample images was conducted using a third custom-written
351 plugin (https://github.com/orion-cirb/Hoechst_ORF1p_pTAU/) developed for the Fiji
352 software, incorporating Bio-Formats and 3D Image Suite libraries. Nuclei detection in the
353 Hoechst channel is performed using the 2D-stitched version of Cellpose (model = 'cyto',
354 diameter = 100, flow threshold = 0.4, cell probability threshold = 0.0, stitching thresh-old =
355 0.5). The resulting 3D nuclei are filtered based on volume, and measurements of nuclei
356 volume, circularity, as well as ORF1p intensity mean and standard deviation are conducted.
357 Circularity is assessed on the middle plane of the nucleus, and intensity measurements are
358 normalized by subtracting the image background noise, as described earlier.
359 If a NeuN channel is provided, NeuN-positive cells detection follows the same process
360 as nuclei detection, with the exception that the model used was trained through the human-in-
361 the-loop procedure implemented in the Cellpose GUI [30]. Specifically, the model was
362 initialized from the 'cyto2' pretrained Cellpose model and trained on 20 images
363 (approximately 50 cells annotated). During the inference phase, the following parameters are
364 employed: diameter = 140, flow threshold = 0.4, cell probability threshold = 0.0, stitching
365 threshold = 0.5. Subsequently, each cell is linked to a nucleus with at least a quarter of its
366 volume in contact with it. Nuclei are thus classified as either NeuN+ or NeuN-.
367
368 **Statistical Analysis**
369 Data were obtained from independent experiments. The number of cells analyzed in each
370 experiment is described in corresponding figure legends. Data analysis was performed using
371 GraphPad Prism 8. Shapiro Wilk normality tests were performed prior to the statistical test to
372 inform whether a parametric or non-parametric test should be used. Statistical tests used are
373 indicated in the figure legends. The significant threshold was defined as $p<0.5$ and depicted as
374 follows on all graphs: *$p < 0.5$, **$p < 0.01$, ***$p < 0.001$, ****$p < 0.0001$.

375

376 **Results**

377

378 **Stress-induced activation of LINE-1 in human post-mitotic dopaminergic neurons**

379 LUHMES cells represent a robust model to investigate the molecular and cellular mechanisms
380 leading to neurodegeneration [31–33]. LUHMES cells were differentiated into post-mitotic
381 neurons according to the experimental paradigm [21–23] displayed in Figure 1A (and Suppl. Fig.
382 1A). These cells acquire a mature dopaminergic neuronal phenotype as revealed by
383 immunostaining for the neuronal marker TuJ1 (β-III tubulin) and the dopaminergic marker
384 TH (Tyrosine hydroxylase) at day 5 of differentiation as shown in Figure 1B (and quantified
385 in Suppl. Fig. 1B). The dopaminergic phenotype of these cells was further confirmed by
386 analyzing TH protein expression by Western blot at different days of differentiation (Suppl.
387 Fig. 1C). Surprisingly, but as previously observed in mouse dopaminergic neurons *in vivo* [5],
388 full-length LINE-1 elements are expressed at steady-state in cultured human dopaminergic
389 neurons as revealed by immunostaining for the LINE-1 ORF1p protein (Fig. 1B). Human
390 ORF1p, as mouse Orf1p [5], shows a predominant cytoplasmic expression pattern but is also
391 observed nuclear. Oxidative stress is a common feature of aging [34–36], cancer [37] and NDs [38–41]
392 and has been associated with LINE-1 activation [42–44]. To generate a human neuronal model of
393 endogenous LINE-1 activation, we induced oxidative stress in differentiated dopaminergic
394 neurons with low-dose arsenite ($NaAsO_2$ ; 50 μM) for 1 hour at day 5 of differentiation as
395 described in Figure 1A. This treatment did not affect the neuronal and dopaminergic
396 phenotypes as shown by TuJ1 and TH immunofluorescence quantification (Suppl. Fig. 1D, E)
397 and triggered no apparent cell death. Oxidative stress increased the expression of LINE-1 in
398 human neurons as revealed by Western blot and immunofluorescence analysis of LINE-1
399 ORF1p protein (Fig. 1C, D). LINE-1 RNA quantification by RT-qPCR using several primers

400 targeting different regions of the LINE-1 sequence also showed an up-regulation of LINE-1
401 transcripts (Suppl. Fig. 1F). In order to test LINE-1 encoded protein activity, we analyzed two
402 known consequences of ORF2p activity (for which no effective antibodies are available).
403 Increased LINE-1 ORF2p has been previously reported to induce DNA damage due to the
404 endonuclease activity [3–5]. Upon oxidative stress, differentiated human dopaminergic neurons
405 displayed increased DNA damage as quantified by an increase in γH2AX (phosphorylated
406 histone H2AX)-positive foci, which decreased in the presence of stavudine, an inhibitor of the
407 reverse transcriptase activity of LINE-1 ORF2p (Fig. 1E). The reverse transcriptase activity of
408 LINE-1 ORF2p has also been reported to generate the accumulation of single-stranded DNA
409 (ssDNA) in the cytosol leading to inflammation [6,45]. We observed an increase of ssDNA foci
410 volume and intensity in the cytosol of stressed neurons (Suppl. Fig. 2A). Full-length LINE-1
411 and its encoded proteins are thus expressed at steady-state in human dopaminergic neurons,
412 are inducible by oxidative stress and functionally active. This *in vitro* model therefore
413 represents a valuable tool to investigate cellular effects of LINE-1 activation mediated by the
414 encoded proteins.
415

416 **ORF1p localizes to the nuclear envelope and translocates into the nucleus upon**
417 **oxidative stress**

418 We next investigated the precise cellular localization and expression levels of ORF1p upon
419 stress using confocal imaging (Fig. 2A). ORF1p was predominantly cytoplasmic both in
420 steady-state as well as in stress conditions and showed both, diffuse and dot-like patterns.
421 Surprisingly and against the current assumptions [46], we observed the presence of ORF1p in
422 the nuclear compartment and an accumulation of ORF1p at the nuclear periphery both at the
423 outer and the inner NE as distinguishable by Hoechst DNA staining (Fig. 2A, B). We further
424 quantified ORF1p intensities using an automated deep-learning based quantification script

425 developed in-house as schematized (Fig. 2C). This script allows for the quantification of
426 immunofluorescence intensities, dot numbers and volumes in pre-defined cellular
427 compartments like the nucleus and the cytosol. The increase in staining intensities in both
428 compartments was accompanied by a rearrangement of staining patterns as revealed by an
429 increase in ORF1p-positive dot numbers and volumes, both in the cytoplasm and the nucleus
430 (Fig. 2D), indicating a possible condensation of LINE-1 ORF1p in stress conditions. As
431 ORF1p appeared to accumulate along the NE, the script was further applied to analyze
432 ORF1p intensity in more detailed compartments including the outer NE, the inner NE and the
433 nucleoplasm (not including the inner NE) (Fig. 2E). The quantification showed a significant
434 increase of ORF1p in both the inner and outer NE and in the nucleoplasm (Fig. 2F).
435 In summary, ORF1p immunostainings using an unbiased image quantification method
436 revealed increased LINE-1 ORF1p levels in the cytoplasm, in the nucleus, and in the inner
437 and outer NE, indicating a general increase of ORF1p, the accumulation of ORF1p at the NE,
438 a rearrangement of ORF1p in a dot-like manner particularly in the cytoplasm and a significant
439 nuclear translocation upon stress.
440
441 **ORF1p targets nuclear envelope components upon oxidative stress**
442 To confirm ORF1p localization to the inner NE, we performed co-immunostainings for
443 ORF1p and Lamin B1, a nuclear lamina protein which decorates the inner NE and plays a key
444 role in the maintenance of nuclear architecture. These experiments revealed the colocalization
445 of ORF1p and Lamin B1 at the inner NE which increased upon stress. This colocalization is
446 particularly visible at the level of lamina invaginations (Fig. 3A). Co-immunoprecipitation
447 experiments confirmed the interaction between ORF1p and Lamin B1 under stress conditions
448 (Fig. 3B). Direct binding of ORF1p to Lamin B1 was further examined by proximity ligation
449 assay (PLA). The results obtained indicate a direct interaction between ORF1p and Lamin B1

450 at the nuclear periphery upon stress (Fig. 3C) in line with the colocalization signals observed
451 by co-immunostainings (Fig. 1A). However, direct interaction of ORF1p and Lamin B1 is
452 also detected in the nucleoplasm of neurons and PLA signal quantification confirmed an
453 increase of the number of dots (= direct interaction events) at the inner NE but also in the
454 nucleoplasmic compartment (Fig. 3D). This suggests a possible scenario in which the stress-
455 induced nuclear translocation of ORF1p and direct ORF1p binding to Lamin B1 induces
456 Lamin B1 mislocalization from the inner NE to the nucleoplasm.

457 Previous studies have shown that ORF1p interacts with importin beta family members
458 (*i.e*, KPNB1) [47,48], which could mediate its nuclear translocation using nuclear pore
459 complexes (NPCs). To confirm that nuclear translocation of ORF1p in neurons upon
460 oxidative stress also mediated by this nuclear import pathway, we performed co-
461 immunostaining of ORF1p with KPNB1 and NUP153 (a nucleoporin of the nuclear basket), a
462 core NPC protein reported to interact with KPNB1 [49,50]. The results shown in Figure 3E
463 indicate the colocalization of ORF1p with KPNB1 and NUP153 at the NE indicating that
464 nuclear translocation of ORF1p in human neurons upon oxidative stress might indeed be
465 mediated by these proteins. In addition, several ORF1p-positive cytoplasmic foci colocalized
466 with KPNB1 (Fig. 3E) which might jeopardize normal KPNB1 function. Direct interaction of
467 ORF1p with KPNB1 and NUP153 was further confirmed by PLA (Fig. 3F). PLA signal of
468 ORF1p and KPNB1 interaction is not affected by oxidative stress (Fig. 3G), whereas the
469 direct interaction between ORF1p and NUP153 is increased in stress condition as indicated by
470 increased number of PLA foci at the inner NE and the nucleoplasm (Fig. 3H). Altogether,
471 these results reveal that ORF1p directly interacts with components of the inner NE and the
472 nucleocytoplasmic transport (NCT) machinery and might interfere with their physiological
473 functions in nuclear architecture and NCT function. This let us to investigate whether ORF1p

474 localization to the NE and direct protein-protein interaction with Lamin B1, KPNB1 and
475 NUP153 might affect NE morphology and/or NCT efficiency.
476
477 **Nuclear ORF1p accumulation correlates with nuclear envelope alterations**
478 Lamin B1 staining of the inner nuclear lamina of human dopaminergic neurons revealed
479 various NE dysmorphologies including nuclear invaginations and blebbing which appeared
480 upon oxidative stress (exemplified in Fig. 4A). It is noteworthy that nearly 70% of stressed
481 cells presented such deformations (Fig. 4B). Co-immunostaining for ORF1p and Lamin B1
482 revealed the accumulation of ORF1p at the level of NE invaginations and blebs, which is
483 clearly observable in STED acquired 3D images (Fig. 4A). Nuclear dysmorphology was
484 accompanied by increased Lamin B1 levels at the inner NE but even more so in the
485 nucleoplasm of stressed cells (Suppl. Fig. 2B), again suggesting a delocalization of Lamin B1
486 possibly as a result of direct protein interaction with ORF1p. The degree of NE distortion
487 (expressed as a circularity index) was analyzed using an automated script (detailed in the
488 Materiel and Methods section) which measures nuclear circularity using Lamin B1 staining as
489 a mask (Fig. 1D). This analysis showed a significant decrease of nuclear circularity in stressed
490 cells (Fig. 4C). Importantly, the degree of nuclear distortion (the lower the index, the higher
491 the distortion) was significantly correlated with the intensity of nuclear ORF1p staining (thus
492 nuclear ORF1p quantity) both in the nucleoplasm ($p<0,0001$; Spearman $r = -0,8230$; 95% CI -
493 0,8578-0,7807) and at the inner NE ($p<0,0001$; Spearman $r = -0,9169$; 95% CI -0,9339-
494 0,8958, Fig. 4E). This correlation suggests that nuclear ORF1p translocation and
495 accumulation in the nucleoplasm and at the inner NE might be involved, at least partly, in the
496 occurrence of nuclear dysmorphologies observed in neurons upon oxidative stress.
497 Human dopaminergic neurons are particularly vulnerable to neurodegeneration
498 observed in PD [51], express ORF1p more abundantly than surrounding neurons and their

499 degeneration can be driven by LINE-1 expression in mice [5]. In addition, NE alterations have
500 been previously described in dentate gyrus brain tissues of sporadic and LRRK2-linked PD
501 samples [52]. In order to establish whether ORF1p is expressed in neurons in the human brain,
502 and if so, whether nuclear ORF1p levels correlate with NE deformations, we turned to human
503 post-mortem brain tissues of PD patients and non-PD affected controls some of whom had
504 signs of early AD pathology (Braak 1-2; Table 1). We chose the cingulate gyrus, a region
505 secondarily affected in PD, reasoning that dopaminergic neurons of the *substantia nigra pars*
506 *compacta*, were most probably already lost at these advanced stages of the disease. We
507 performed immunostainings using ORF1p, the pan-neuronal marker NeuN and either Hoechst
508 to identify the nucleus or Lamin A/C to identify the NE and used an unbiased machine-
509 learning assisted cell detection workflow which (a) identifies neurons based on the presence
510 of NeuN, (b) delimits the nucleus based on Hoechst staining, (c) quantifies ORF1p within this
511 delimitation and (d) measures the circularity of the nuclei. Immunostainings of ORF1p and
512 Lamin A/C or Hoechst show a mostly cytoplasmic but also nuclear localization of ORF1p in
513 neurons in samples from both, PD patients and non-PD controls (Fig. 4F, G). Importantly,
514 analysis of a correlation of nuclear ORF1p intensity with nuclear circularity in each identified
515 neuron identified a significantly negative correlation between the two parameters in PD
516 samples (p=0.0021; Spearman r= - 0.1949; 95% CI -0.32-0.07) but not in controls (p= 0.4725;
517 Spearman r = -0.06458; 95% CI -0.24-0.12, Fig. 4H). As in human dopaminergic neurons in
518 culture, this suggests a relationship in human post-mortem neurons in which the higher the
519 concentration of ORF1p, the more pronounced the deformation of the nucleus.

520 In an attempt to establish causality between an increase in nuclear ORF1p and nuclear
521 dysmorphologies, we used siRNA to knock-down LINE-1 expression. However, this
522 approach did not significantly decrease nuclear ORF1p. We therefore turned to a different
523 approach by blocking nuclear import of ORF1p using nuclear import inhibitors. As

524 mentioned above, ORF1p nuclear import is mediated by a KPNB1/KPNA2-dependent
525 process [47,48]. KPNA2 is an importin alpha family member, which recognizes NLS of cargo
526 proteins and serves as an adapter for KPNB1 for the import activity of the complex. KPNA2
527 has been shown to be involved in nuclear import of ORF1p in addition to KPNB1 [47,48]. Using
528 ivermectin, a KPNB1 inhibitor [53,54], and importazole, an inhibitor of KPNA2 [55,56], we
529 obtained a significant decrease in nuclear ORF1p upon stress (Fig. 5A), which we did not
530 observe with either drug alone (Suppl. Fig. 2C, D). ORF1p nuclear import in human neurons
531 is thus dependent on both, KPNB1 and KPNA2. Importantly, the decrease in nuclear
532 circularity upon stress was significantly rescued by blocking the import of ORF1p into the
533 nucleus (Fig. 5A). Therefore, the correlation of an increase of nuclear ORF1p with a decrease
534 in nuclear circularity as well as the restoration of nuclear deformations by blockade of ORF1p
535 nuclear import in stress conditions strongly indicates that nuclear ORF1p causally participates
536 in the loss of NE integrity. It is noteworthy that ORF2p reverse transcriptase inhibitor
537 (stavudine) which prevented ORF2p induced DNA strand breaks (Fig. 1E) did not have any
538 effect on nuclear circularity, or Lamin B1 delocalization, nor on ORF1p nuclear and
539 cytoplasmic levels (Suppl. Fig. 3A-C). This indicates that the effect observed is not due to
540 ORF2p activity.

541 Since nuclear lamina plays an important role in anchoring heterochromatin at the inner
542 NE (= nuclear lamina), we examined whether the observed alteration of the nuclear lamina is
543 accompanied by heterochromatin disorganization by immunostaining for the heterochromatin
544 markers HP1 (heterochromatin protein-1) and the repressive histone mark H4K20me3
545 (histone H4 trimethylated on lysine 20) in control and stressed cells. HP1 was significantly
546 depleted from the inner NE (Fig. 5B) and H4K20me3 levels decreased in stress conditions
547 (Fig. 5C) suggesting possible decondensation or detachment of heterochromatin from the
548 inner NE and favoring conditions allowing the activation of LINE-1 expression [57].

549

550 **Nuclear envelope targeting by ORF1p is accompanied by nucleocytoplasmic transport**
551 **defects**

552 In view of the interaction of ORF1p with KPNB1 and NUP153 reported above, we examined
553 whether the accumulation of ORF1p at the NE could lead to NCT deficiencies.
554 Immunostainings and subsequent quantification of intensity, distribution and localization of
555 KPNB1 showed an accumulation of KPNB1 in the cytoplasm, as revealed by an increase in
556 the intensity of KPNB1. We also observed a change in KPNB1 distribution, as revealed by an
557 increase in the number of counted dots and their volume in the cytoplasm (Fig. 6A) indicating
558 a possible alteration of its function. To examine whether these changes in KPNB1 upon stress
559 were associated with NCT defects, we first analyzed the localization of a major
560 nucleocytoplasmic transport protein, RanGAP1, by immunostaining. The GTPase activity of
561 this protein is involved in maintaining the Ran gradient required for NCT and its
562 delocalization is associated with NCT defects [58]. RanGAP1 accumulated in the cytoplasm,
563 shown by increased intensity, number and dot volume in the cytoplasm (Fig. 6B) which is
564 indicative of an alteration of NCT. Disruption of NCT can lead to the abnormal localization of
565 the RNA binding protein TDP-43 (TAR DNA-binding protein 43) , a predominantly nuclear
566 protein. Mutations in TDP-43 gene (*TARDBP*) are causal in familial forms of FTD
567 (Frontotemporal dementia) and ALS and a change from its predominantly nuclear to
568 cytoplasmic localization has been observed in several NDs [59,60]. Current consensus suggests
569 that TDP-43 misdistribution leads to a pathological gain-of-function in the cytoplasm and
570 loss-of-function in the nucleus [61,62] contributing to cellular dysregulation culminating in
571 neurodegeneration. We therefore performed immunostainings for TDP-43 which revealed the
572 presence of TDP-43-positive foci in the cytoplasm under stress conditions which were absent
573 in non-stressed controls. Quantification showed that the intensity as well as the number and

574 volume of TDP-43 positive dots were increased in the cytoplasm in stressed neurons (Fig.
575 6C). NUP153 is a nucleoporin which is involved in NCT and its cytoplasmic mislocalization
576 and/or intranuclear accumulation are associated with NCT defects in various
577 neurodegenerative contexts [58,63,64]. The quantification of NUP153 showed an abnormal
578 intranuclear and cytoplasmic accumulation of NUP153 in stress conditions (Fig. 6D).
579

580 **ORF1p overexpression leads to nuclear envelope dysmorphology and nucleocytoplasmic**
581 **transport defects in the absence of oxidative stress**

582 In order to evaluate whether NE dysmorphology induced by an increase in nuclear ORF1p
583 could also be observed in the absence of arsenite-induced stress, we performed gain of
584 function experiments by nucleofection of a plasmid expressing HA-tagged ORF1p but not
585 ORF2p. Dopaminergic neurons were nucleofected at day 3 of differentiation with a plasmid
586 encoding either HA-ORF1 or GFP control and analyzed 48 h later. Co-immunostainings for
587 HA and Lamin B1 showed the presence of HA-ORF1 in the nucleus and at the inner NE,
588 colocalizing with Lamin B1 (Fig. 7A). HA-ORF1 transfected cells displayed pronounced NE
589 deformations as revealed by Lamin B1 staining (Fig. 7A), decreased circularity and increased
590 nucleoplasmic Lamin B1 levels compared to GFP expressing cells (Fig. 7B). Interestingly,
591 nuclear circularity was highly correlated with the nuclear intensity of HA-ORF1 in transfected
592 cells (Fig. 7B), strongly suggesting a link between ORF1p nuclear localization and NE
593 dysmorphology. Neurons transfected with HA-ORF1 also presented increased levels of
594 RanGAP1 in the cytoplasm and TDP-43 in both the cytoplasm and nucleus compared to GFP
595 expressing cells (Fig. 7C-F). These results indicate that overexpression of ORF1p, in the
596 absence of stress, is sufficient to induce NCT defects and NE dysmorphology in human
597 dopaminergic neurons and again establish a causal link between NE abnormalities and nuclear
598 ORF1p content.

599

600 **Rescue of nuclear envelope dysmorphology under stress conditions by remodelin**

601 NE morphology is disrupted during aging [65] and in premature aging syndromes caused by
602 laminopathies [66,67] including progeria syndromes [68]. In Hutchinson-Gilford progeria syndrome
603 (HGPS), nuclear integrity was shown to be restored by the small molecule remodelin, an
604 inhibitor of the acetylase-transferase protein NAT10 [69]. But whether this molecule is efficient
605 in restoring misshapen nuclear morphology in cell types other than fibroblasts or epithelial
606 cells was not known. We therefore examined whether NE dysmorphology induced by ORF1p
607 under oxidative stress in human neurons could be restored by remodelin. NE deformations (i.e
608 invaginations) were clearly restored in cells pre-treated with remodelin for 24 h (Fig. 8A, B).
609 Quantification showed that the decrease of nuclear circularity following arsenite treatment
610 was restored by remodelin (Fig. 8B), which was paralleled by a reduction of nucleoplasmic
611 Lamin B1 levels quantified in Figure 8B. In order to investigate whether remodelin treatment
612 had an influence on ORF1p levels, we performed ORF1p immunostainings on cells treated or
613 not with remodelin. Arsenite-induced nuclear ORF1p increase was completely normalized in
614 the presence of remodelin, both at the inner NE and in the nucleoplasm (Fig. 8C)
615 Interestingly, in these conditions cytoplasmic ORF1p levels remained unchanged at an
616 expected higher level than non-stressed controls. Since remodelin has been reported to restore
617 a "juvenile" chromatin state in Progeria models [69,70], we examined H4K20me3, known to
618 repress LINE-1 elements [57,71]. As shown in Figure 8A, H4K20me3 immunostaining was
619 significantly decreased following stress and restored with remodelin treatment as confirmed
620 by quantification of H4K20me3 intensity in the nucleus (Fig. 8D). This suggests that the
621 decrease of nuclear ORF1p upon remodelin treatment in stressed cells might induce indirect
622 blockade of nuclear ORF1p translocation. Alternatively, this decrease could also be due to a

623 transcriptional inhibition of LINE-1 or a consequence of deposition of H4K20me3 at LINE-1
624 loci.
625
626
627 **Discussion**
628 In recent years, TEs have emerged as possible new pathogenic players in NDs [5,10,13,19,20,72–74].
629 However, the mechanisms through which LINE-1 might contribute to the pathogenesis of
630 NDs still remain poorly understood potentially implicating cis-genetic or epigenetic, LINE-1
631 RNA or LINE-1 protein-mediated effects. Concerning the latter, the study of potential
632 pathogenic effects of LINE-1 ORF2p has received most attention due to its enzymatic
633 activities as an endonuclease and reverse transcriptase while ORF1p has widely been reduced
634 to an RNA chaperone with cis-preference for its own RNA and a necessary component of the
635 LINE-1 ribonucleoprotein particle (RNP) for retrotransposition. Previous work suggests that
636 ORF2p is not only a source of genomic instability [3–6,20], but can also trigger the innate
637 immune response through reverse transcription of RNA generating cytoplasmic ssDNA [6,8,45].
638 While ORF2p reverse transcriptase activity can be targeted by inhibitors (nucleoside reverse
639 transcriptase inhibitors, NRTIs, i.e., stavudine), the analysis of ORF2p protein expression and
640 localization remains challenging due to a lack of efficient antibodies and/or its lesser
641 abundance compared to ORF1p (1 ORF2p for 240 ORF1p molecules per LINE-1 RNP [75]). In
642 contrast, no inhibitor has been identified to target ORF1p activity, but effective antibodies are
643 available to explore its expression and subcellular localization in pathological situations.
644 However, a better understanding of the implication of ORF1p in the LINE-1 life cycle and
645 beyond is important as accumulating data suggests that full-length LINE-1 are expressed,
646 predominantly in epithelial cancers [76] but also at steady-state in mouse neurons [5], human
647 neurons [77] and post-mortem brain tissues [78].

648 Using a human neuronal model of oxidative stress which displays increased LINE-1
649 activity as monitored by an increase in ORF1p expression and ORF2p-dependent genomic
650 instability, we observed not only an increase of ORF1p in the cytoplasm, but also a striking
651 translocation of ORF1p to the nucleus. Current consensus postulates that LINE-1 encoded
652 proteins enter the nucleus only during cell cycle [46] which thus would exclude the presence of
653 LINE-1 proteins in the nucleus of non-dividing cells including post-mitotic neurons.
654 However, others have reported the presence of ORF1p in the nucleus of human cells in a
655 neurodegenerative context [79] and in post-mortem human brain tissues [78]. We also observed
656 ORF1p staining in the nucleus of human dopaminergic neurons *in vitro* and in mouse
657 dopaminergic neurons *in vivo* even at steady-state [5], and oxidative stress dramatically
658 increases the nuclear translocation of ORF1p. The most probable mode of import for ORF1p
659 is the importin-beta pathway. Indeed, ORF1p, as we show here in neurons and others have
660 shown in HeLa cells [47] binds directly to the importin alpha and beta family members, KPNA2
661 and KPNB1, which are transport proteins carrying cargo proteins through the NPC. This
662 importin-assisted mode of nuclear entry is widely used by several viral proteins [80,81], certain
663 retrotransposons (i.e Ty1 [82], LINE-1 ORF1p itself [48]) but also a pathological form of Tau
664 which aggregates in neurodegeneration [83]. The binding of ORF1p to KPNB1 does not
665 increase under stress condition indicating that the stress-induced increase of ORF1p nuclear
666 translocation probably requires other protein partners. It is noteworthy that ORF1p, in a
667 stress-dependent manner, accumulates both at the outer NE and the inner NE which
668 corresponds to the nuclear lamina and co-localizes with and binds directly to the NPC protein
669 NUP153. This suggests a NUP153-dependent nuclear import of ORF1p under stress.
670 The small transcriptional increase in LINE-1 RNA following arsenite treatment
671 suggests that the overall increase in ORF1p could be partially transcriptional and partially
672 post-transcriptional, possibly by releasing LINE- 1 RNA stored in P-bodies for translation

673 [84,85]. Once ORF1p translocates to the nucleus, it accumulates at the inner NE by directly
674 binding to Lamin B1 in a stress-specific manner. This targeting of the inner NE by ORF1p is
675 paralleled by NE dysmorphology including invaginations and blebs which significantly
676 correlated with ORF1p intensity, both in the nucleus and the inner NE, suggesting that it is the
677 stress-dependent nuclear translocation of ORF1p and the direct binding to Lamin B1 that
678 participate in NE dysmorphology. This conclusion is also supported by the fact that nuclear
679 dysmorphologies under oxidative stress are prevented when ORF1p nuclear import is blocked
680 by nuclear import inhibitors or, through unknown mechanisms, by remodelin.

681 A direct functional role of ORF1p in NE dysmorphology independent of oxidative
682 stress is further supported by direct ORF1p gain of function experiments showing that
683 neurons over-expressing ORF1p (and not ORF2p) display a significant decrease of nuclear
684 circularity. These experiments also suggest that NE dysmorphology is mediated by the
685 nuclear presence of ORF1p alone and does not rely on the presence of the entire RNP or
686 ORF2p.

687 NE dysmorphology is associated with NCT deficiencies [86] and both have been
688 described to be disturbed in the context of NDs [52,62,63,87–91]. Indeed, targeting of the NE by
689 ORF1p in neurons was accompanied by NCT deficiencies as revealed by the mislocalization
690 and abnormal and compartmentalized accumulation of several proteins involved in NCT
691 function, some of which interact with ORF1p directly (KPNB1 and NUP153). KPNB1
692 sequestration by binding to ORF1p might alter nuclear import but could also inhibit its
693 important disaggregase function [92]. Analogous, the abnormal localization of NUP153 in the
694 nucleoplasm suggests an alteration of its physiological function, potentially mediated by the
695 interaction with ORF1p as illustrated by the accumulation of nucleoplasmic PLA foci.
696 Nucleoporins are long-lived proteins [93,94] and rely on cell division for their renewal. Post-
697 mitotic neurons do not divide and nucleoporins therefore are not renewed [95,96]. Their

698 continuous functioning in non-dividing cells throughout the life time of an individual is thus
699 of crucial importance and any perturbations will have potentially irreversible consequences [95].
700 Abnormal intranuclear and cytoplasmic accumulation of certain nucleoporins as we observed
701 for NUP153 in stressed neurons has also been described in the context of other NDs (i.e, HD)
702 [91]. Possible cytoplasmic sequestration of NUP98 by tau has also been suggested to lead to
703 NCT perturbation in AD [97]. Similarly, delocalization and abnormal cytoplasmic accumulation
704 of RanGAP1 we observed in stressed neurons, have also been described in several ND-
705 affected tissues [58]. Our results suggest that ORF1p might act as a sponge to alter the activity
706 of certain proteins involved in NCT. Together, our results suggest a possible scenario in
707 which ORF1p might sequester and/or mislocalize NE components such as Lamin B1 or
708 NUP153 (see below).

709 NCT deficiencies have been consistently linked to the abnormal subcellular
710 distribution of TDP-43, a nuclear protein involved in RNA metabolism [98,99], mutated in
711 ALS/FTD [100–103] and mislocalized to the cytoplasm in numerous NDs [58,61,62] not linked to
712 TDP-43 mutations. Indeed, in our model, NCT deficiencies as a consequence of mislocalized
713 NCT proteins resulted in the cytoplasmic accumulation of TDP-43. TDP-43 exits the nucleus
714 through passive [104] or active nuclear export [105] through nuclear pores. We also observed an
715 increase in the nuclear pool which could be indicative of a perturbed export mechanism of
716 this shuttling protein [106].

717 NE alteration and NCT defects are emerging pathogenic features in several NDs
718 [87,97,107] including HD [90], ALS/FTD [63], PD [52], AD [97,107] and more generally in the context of
719 tauopathies [108]. For example, aggregated Tau directly interacts with the nuclear pore complex
720 [97] and oligomeric Tau with lamin proteins [109] resulting in loss of nuclear integrity including
721 NCT failure [86], similar to what we describe here. Loss of nuclear integrity in the form of NE
722 deformation and loss of NE function has been extensively described in the context of aging [110]

723 including in the brain [111] with associated changes in chromatin organization and NCT
724 dysfunction [107,111–113]. Progerin, a mutant form of Lamin A, is the cause of HGPS. Similar to
725 mutant Tau, it accumulates at the NE and disrupts NE morphology, NCT and chromatin
726 organization [69]. In cellular and mouse models of accelerated aging, these alterations can be
727 successfully corrected by treatment with the small molecule remodelin [69,70]. Remodelin acts
728 by inhibiting the acetyltransferase NAT10 [69]. In our model of oxidative stress, pre-treatment
729 of neurons with remodelin 24 h prior to arsenite application restored, just as in progeria cells,
730 NE abnormalities. In parallel, remodelin decreased nuclear ORF1p while not affecting
731 cytoplasmic ORF1p content. Remodelin might thus, through the restoration of the nuclear
732 architecture, prevent ORF1p nuclear translocation and therefore further ORF1p-induced NE
733 dysmorphology. Nuclear lamina-alterations do not only affect NCT but alter global chromatin
734 organization [114] and potentially cell type specific gene expression [115]. Chromatin organization
735 in cells is spatial and specific heterochromatin domains are directly linked to the nuclear
736 lamina, called lamina-associated domains (LADs). One marker associated with LADs is
737 H4K20me3, a repressive heterochromatin mark known to silence LINE-1 elements [57]. Indeed,
738 oxidative stress induced a global loss of H4K20me3 which is rescued by remodelin pre-
739 treatment. Together, these data indicate that remodelin can preserve and/or restore nuclear
740 integrity of neurons including chromatin disorganization induced by oxidative stress possibly
741 or at least partly through an inhibitory effect on ORF1p nuclear translocation. The
742 destructuration of nuclear lamina-anchored heterochromatin as indicated by the delocalization
743 of H4K20me3 from the nuclear periphery could lead to the expression of genes normally
744 repressed in post-mitotic neurons leading to neuronal fate loss, an emerging feature of aging
745 and NDs [116]. Indeed, mutated Tau can lead to chromatin relaxation, re-expression of certain
746 fetal genes in the brain in a fly model [18] and activation of TEs [14,18]. Further, the loss of
747 H4K20me3 at the nuclear periphery could either be the source of LINE-1 activation (as

748 H4K20me3 is a repressive mark known to decorate repeat DNA [117,118]) or the consequence of
749 nuclear ORF1p translocation leading to a decrease in H4K20me3 through a yet to be
750 identified mechanism. This would indeed lead to the amplification of the initial stress-induced
751 increase in LINE-1 via a positive feedback loop. Another possibility is an adaptive response
752 aimed at protecting the genome from damage as a short-term response to deformation [119–121].

753 Recent studies have shown that aggregated proteins such as Tau [83,122], mutant
754 Huntingtin [90] and C9orf72 poly-GA proteins [58] can target the NE and alter its integrity and
755 function. Our data suggests that ORF1p might have a pathogenic action similar to ND-linked
756 proteins by perturbing nuclear integrity. In addition, stress-granule independent cytoplasmic
757 TDP-43 droplets can drive nuclear import defects and cell death [123]. Whether nuclear import
758 defects are driven by a direct ORF1p dependent mechanism or via ORF1p-dependent TDP-43
759 cytoplasmic accumulation remains to be determined.

760 Condensation is a feature of ORF1p which is intrinsic to its role in LINE-1
761 mobilization [124]. We observed large ORF1p foci at the level of NE invaginations and an
762 increase in the size of cytoplasmic and nuclear ORF1p foci (dots) indicative of ORF1p
763 condensation. Whether ORF1p itself might be aggregation-prone or participate in the
764 organization of LLPS (Liquid-liquid phase separation)-related cytoplasmic or nuclear
765 membraneless organelles requires further investigation.

766 Altogether, we provide evidence that the LINE-1 encoded protein ORF1p,
767 independent on the LINE-1 RNP or ORF2p, translocates to the nucleus upon cellular stress or
768 overexpression in an importin-beta and NUP153 involving process. Upon translocation,
769 ORF1p binds to Lamin B1 and sequesters and/or mislocalizes this protein, which is essential
770 to NE integrity, leading to further deformation of the NE. In parallel, while entering the
771 nucleus through nuclear pores, ORF1p binds to NUP153, leading to its mislocalization to the
772 nucleoplasm and the cytoplasm and thereby contributing to NCT deficiencies including the

773 cytoplasmic accumulation of TDP-43. Nuclear localization and the correlation of ORF1p
774 nuclear intensity with the loss of nuclear circularity in neurons of PD patients suggest that
775 ORF1p might fulfil a similar pathological function in neurodegenerative disease.

776 NE deformation is associated with chromatin disorganization as illustrated by HP1
777 loss at the inner NE and global H4K20me3 depletion in the nucleus. Nuclear deformation and
778 chromatin disorganization upon cell stress were rescued by the small molecule remodelin
779 which might indirectly act as an inhibitor of ORF1p nuclear translocation. This suggests that
780 LINE-1 encoded protein ORF1p, for which no pathogenic function had yet been assigned,
781 might play a pathogenic role by targeting the NE. As LINE-1 activation is a recurring
782 observation in several neurological diseases [125–131], in aging [6] and more generally upon
783 oxidative stress [5] and if this activation includes full-length LINE-1 elements with coding
784 potential, the result could be an increase in ORF1p, in addition to ORF2p and LINE-1 RNA.
785 Passing a certain threshold and in conjunction with a fragilization of the NE either through
786 aging, ND-linked mutated proteins known to affect the NE or oxidative stress, this then might
787 trigger the nuclear translocation of ORF1p contributing to NE deformation and NCT
788 dysfunction. One consequence we identified is the cytoplasmic accumulation of TDP-43
789 which could favor its aggregation [132], one of the hallmarks of several NDs [58,61,62].

790 Activation of LINE-1 elements in neurons, through ORF2p-induced genomic instability [5],
791 ORF2p-induced inflammation [6,8,45] or LINE-1 RNA mediated heterochromatin erosion [133]
792 and, as we show here, through the ORF1p-dependent fragilization of nuclear integrity could
793 contribute in multiple ways to pathological features common to several NDs. This reinforces
794 the idea that LINE-1 elements might represent a novel therapeutic target for neuroprotection.

795

796 **Acknowledgements**

RZ acknowledges the Fondation Recherche Alzheimer (FRA) for a Ph.D. fellowship and is enrolled with the Ecole Doctorale ED3C at Sorbonne University. We are very grateful to Raphaël Rodriguez and Ludovic Colombeau for having synthetized and provided the small molecule remodelin. This work was supported by grants to JF from the Fondation de France (00086320), the Fondation du Collège de France, the Fondation NRJ/Institut de France, the National French Agency for Research (ANR-20-CE16-0022 NEURAGE) and the Fondation Alzheimer. We gratefully acknowledge Julien Dumont and the Collège de France Orion imaging facility (IMACHEM-IBiSA), member of the French National Research Infrastructure France-BioImaging (ANR-10-INBS-04), which received support from the program «Investissements d'Avenir» ANR-10-LABX-54 MEMOLIFE. We also thank the Fondation Bettencourt Schueller for their support. Human post-mortem brain material and associated data were obtained from the "Brainbank Neuro-CEB Neuropathology Network" which is supported by ARSLA, CSC, France DFT, Fondation ARSEP, Fondation Vaincre Alzheimer, France Parkinson.

**Author contributions**

RZ performed most of the experiments. OMB contributed experimentally, PM and HM wrote the scripts for the automated image analysis workflow, RLJ and JF supervised the study and wrote the paper with RZ. JF received the funding.

**Figure Legends**

**Figure 1. LINE-1 are upregulated in differentiated LUHMES cells following stress.**

(A) Experimental paradigm of the differentiation scheme of LUHMES neuronal precursor cells into mature, post-mitotic dopaminergic neurons. At day 5 of differentiation, neurons

822 were subjected to an oxidative stress using arsenite ($NaAsO_2$). (B) After 5 days of
823 differentiation, LUHMES cells express the neuronal marker TuJ1 and the dopaminergic
824 marker TH as revealed by immunofluorescence. These neurons express LINE-1 at steady-
825 state as shown by immunostaining for ORF1p protein. (C) Differentiated LUHMES neurons
826 subjected to arsenite treatment, show increased levels of ORF1p protein by Western blot
827 analysis. n = 3 wells per condition from 4 independent experiments, mean ± SEM, two-tailed t
828 test. (D) Immunostaining for LINE-1 ORF1p of differentiated LUHMES cells treated with
829 arsenite and quantification of global ORF1p intensity, n > 100 neurons were quantified per
830 condition, a representative experiment (3 wells per condition) of 3 independent experiments,
831 mean ± SEM, two-tailed t test. (E) Immunostaining of γH2AX following arsenite treatment in
832 the presence or the absence of stavudine and quantification of γH2AX foci number in the
833 nucleus. n > 100 neurons were quantified per condition, a representative experiment (3 wells
834 per condition) of 2 independent experiments, mean ± SEM, One-way ANOVA with Tukey's
835 multiple comparisons test (*p < 0.5, **p < 0.01, ***p < 0.001, ****p < 0.0001. (Also see
836 supplementary Fig. 1). Scale bar, 5 µm.
837
838 **Figure 2. ORF1p increases, changes its conformational pattern and translocates to the**
839 **nucleus following oxidative stress.**
840 (A) Immunostaining for LINE-1 ORF1p of differentiated LUHMES cells treated with
841 arsenite. (B) Quantification of ORF1p intensity both in the cytoplasm and the nucleus in the
842 presence and the absence of stress. n > 100 neurons were quantified per condition, a
843 representative experiment (3 wells per condition) of 8 independent experiments, mean ±
844 SEM, two-tailed t test (C) Scheme of the script (for details see Materials and Methods) for
845 ORF1p quantification in the cytoplasmic, nuclear (nucleoplasm = nucleus – inner NE) and
846 inner and outer NE compartments. (D) Quantification of the number and volume of ORF1p

847 positive dots shown in ROI (region of interest) (A) in the cytoplasm and the nucleus using the
848 same script, n > 100 neurons were quantified per condition, a representative experiment (3
849 wells per condition) of 8 independent experiments, mean ± SEM, two-tailed t test.
850 (F) Quantification of ORF1p signal at the NE by an in-house script as schematized in (E) (for
851 details see Materiel and Methods) shows increased ORF1p intensity at the inner NE, outer NE
852 and in the nucleoplasm, n > 100 neurons were quantified per condition, a representative
853 experiment (3 wells per condition) of 5 independent experiments, mean ± SEM, two-tailed t
854 test (*p < 0.5, **p < 0.01, ***p < 0.001, ****p < 0.0001. Scale bar, 5 µm.
855
856 **Figure 3. ORF1p association with nuclear envelope components and nuclear transport**
857 **proteins increases upon oxidative stress.**
858 (A) Co-immunostaining of ORF1p and Lamin B1 reveals their colocalization (yellow). (B)
859 Validation of ORF1p interaction with Lamin B1 by co-immunoprecipitation and Western-
860 blotting. (C) Direct interaction of ORF1p with Lamin B1 was revealed by PLA and quantified
861 in (D), n > 50 neurons were quantified per condition, (3 wells per condition). (E) Co-
862 immunostaining of ORF1p and KPNB1 or NUP153. (F) Validation of a direct interaction
863 between ORF1p and KPNB1 or NUP153 by PLA. The quantification in separate cellular
864 compartments is shown in (G, H), n > 50 neurons were quantified per condition, (3 wells per
865 condition), mean ± SEM, two-tailed t test (*p < 0.5, **p < 0.01, ***p < 0.001, ****p <
866 0.0001). Scale bar, 5 µm.
867
868 **Figure 4. Stress induced association of ORF1p to the nuclear envelope leads to nuclear**
869 **envelope dysmorphology.**
870 (A) NE dysmorphology in the arsenite stress model revealed by co-immunostaining of ORF1p
871 and LaminB1 quantified in (B). The percentage of deformed cells was quantified in > 10

872 images per condition, a representative experiment (3 wells per condition) of 3 independent
873 experiments is shown, mean ± SEM, two-tailed t test. (C) Quantification of nuclear
874 dysmorphology by analyzing nuclear circularity using a dedicated script (for details see
875 Materiel and Methods) based on Lamin B1 as a mask (D), shows decreased circularity under
876 stress conditions. n > 100 neurons were quantified per condition, a representative experiment
877 (3 wells per condition) of 5 independent experiments, mean ± SEM, two-tailed t test. (E)
878 Correlation of ORF1p intensity per cell in the nucleus or at the inner NE with nuclear
879 circularity. n > 100 neurons were quantified per condition, a representative experiment (3
880 wells per condition) of 3 independent experiments; Spearman correlation (*p < 0.5, **p <
881 0.01, ***p < 0.001, ****p < 0.0001). (F) Co-immunostaining of ORF1p and Lamin A/C in
882 neurons of the cingulate gyrus of post-mortem PD and non-PD tissues. (G) Immunostaining
883 of NeuN, Lamin A/C and ORF1p in the cingulate gyrus of post-mortem PD and non-PD
884 tissues. (H) Correlation of nuclear ORF1p intensity and circularity per NeuN-positive cell in
885 the cingulate gyrus of post-mortem tissues from PD patients (n = 5) and non-PD affected
886 individuals (n = 4); Spearman correlation (*p < 0.5, **p < 0.01, ***p < 0.001, ****p <
887 0.0001).
888
889 **Figure 5. Restauration of nuclear circularity upon blockade of ORF1p nuclear import**
890 **and analysis of chromatin repressive marks upon stress.**
891 (A) Quantification of ORF1p nuclear intensity and the nuclear circularity in the presence or
892 the absence of import inhibitor drugs ivermectin (IV) and importazole (IMP) in stressed and
893 control cells. n > 100 neurons were quantified per condition, a representative experiment (3
894 wells per condition) of 2 independent experiments, mean ± SEM, One-way ANOVA with
895 Tukey's multiple comparisons test. (B) Immunostaining of HP1 in stressed cells and the ratio
896 of HP1 intensity in the nucleoplasm over the nuclear periphery (inner NE). n > 100 neurons

897 were quantified per condition, a representative experiment (3 wells per condition) of 3
898 independent experiments, mean ± SEM, two-tailed t test. (H) Immunostaining of H4K20me3
899 repressive histone mark in stressed and control cells and its quantification in the nucleus. n >
900 100 neurons were quantified per condition, a representative experiment (3 wells per
901 condition) of 3 independent experiments, mean ± SEM, two-tailed t test (*p < 0.5, **p < 0.01,
902 ***p < 0.001, ****p < 0.0001). Scale bar, 5 µm.
903
904 **Figure 6. Stress induced association of ORF1p with the nuclear envelope is accompanied**
905 **by nucleocytoplasmic transport defect.**
906 (A) Immunostaining of KPNB1 in oxidative stress conditions and quantification of the
907 intensity levels, the number and the volume of dots in the cytoplasm. (B) Immunostaining of
908 NPC protein RanGAP1 in oxidative stress conditions and quantification of the intensity
909 levels, the number and the volume of dots in the cytoplasm. (C) Immunostaining of TDP-43
910 in oxidative stress conditions and quantification of the intensity levels, the number and the
911 volume of dots in the cytoplasm. (D) Immunostaining of NUP153 in oxidative stress
912 conditions and quantification of the intensity levels in the nucleoplasm and the cytoplasm. n >
913 100 neurons were quantified per condition, a representative experiment (3 wells per
914 condition) of 3 independent experiments, mean ± SEM, two-tailed t test (*p < 0.5, **p < 0.01,
915 ***p < 0.001, ****p < 0.0001). Scale bar, 5 µm.
916
917 **Figure 7. LINE-1 over-expression following transfection leads to nuclear envelope**
918 **deformation and nucleocytoplasmic transport defects in the absence of stress.**
919 (A) Co-Immunostaining of HA and Lamin B1 in cells transfected with pcDNA3-ORF1-HA or
920 with pmaxGFP as a control. (B) Quantification of the nuclear circularity index, Lamin B1
921 intensity in the nucleoplasm (left panel; mean ± SEM, two-tailed t test) and correlation of

922 HA-ORF1p intensity per cell in the nucleus with nuclear circularity (right panel; Spearman
923 correlation). n > 90 neurons were quantified per condition, a representative experiment (3
924 wells per condition) of 3 independent experiments; (*p < 0.5, **p < 0.01, ***p < 0.001,
925 ****p < 0.0001). (C) Immunostaining of HA and RanGAP1 in cells transfected with
926 pcDNA3-ORF1-HA or with pmaxGFP as a control. (D) Quantification of cytoplasmic
927 RanGAP1 intensity in transfected cells with pcDNA3-ORF1-HA or pmaxGFP as a control. n
928 > 90 neurons were quantified per condition (3 wells per condition), mean ± SEM, two-tailed t
929 test. (E) Immunostaining of HA and TDP-43 in cells transfected with pcDNA3-ORF1-HA or
930 with pmaxGFP as a control. (F) Quantification of cytoplasmic and nuclear TDP-43 signal in
931 cells transfected with pcDNA3-ORF1-HA or pmaxGFP as a control. n > 100 neurons were
932 quantified per condition (3 wells per condition), mean ± SEM, two-tailed t test (*p < 0.5, **p
933 < 0.01, ***p < 0.001, ****p < 0.0001). Scale bar, 5 µm.
934
935 **Figure 8. Restauration of nuclear alterations by the small molecule remodelin**
936 (A) Immunostaining of ORF1p, Lamin B1 and H4K20me3 of neurons with or without
937 remodelin pre-treatment 24 h before addition of arsenite or sham. (B) Quantification of
938 nuclear circularity and Lamin B1 intensity in the nucleoplasm. (C) Quantification of ORF1p
939 intensity in the nucleus, in the inner NE and in the cytoplasm. (D) Quantification of
940 H4K20me3 intensity in the nucleus. n > 100 neurons were quantified per condition, a
941 representative experiment (3 wells per condition) of 3 independent experiments, mean ±
942 SEM, One-way ANOVA with Tukey's multiple comparisons test (*p < 0.5, **p < 0.01, ***p
943 < 0.001, ****p < 0.0001). Scale bar, 5 µm.
944
945
946

947 **Table 1. List of PD and non-PD post-mortem tissues used in this study.**

| Internal ID | Diagnosis | PMI (hr) | Gender | Age at death | Pathological staging |
|---|---|---|---|---|---|
| 6629 | Parkinson Disease | 35 | M | 72 | Diffuse Lewy Body Disease |
| 8418 | Parkinson Disease | 36 | M | 82 | Diffuse Lewy Body Disease |
| 7826 | Parkinson Disease | nd | F | 62 | Diffuse Lewy Body Disease |
| 6532 | Parkinson Disease | 48 | F | 94 | Diffuse Lewy Body Disease |
| 3771 | Parkinson Disease | 20 | M | 83 | Diffuse Lewy Body Disease |
| | | 34.8 (+/-11.2) | 2F / 3M | 78.6 (+/-12.1) | |
| 6203 | Non-PD | 23 | M | 78 | Alzheimer lesion Braak II |
| 8866 | Non-PD | 15 | M | 84 | - |
| 4078 | Non-PD | 10 | M | 73 | Alzheimer lesion Braak II |
| 5603 | Non-PD | 21 | F | 92 | Alzheimer lesion Braak I |
| 7197 | Non-PD | 10 | M | 85 | Alzheimer lesion Braak II |
| | | 15.8 (+/-6.1) | 3F/ 4M | 82.4 (+/-7.2) | |

948 PMI, post-mortem interval.

949

950

951

952

953

954

955

956

957

958

959

960

961

962

963

964

965

966 **References**

967


968 1. International Human Genome Sequencing Consortium, Whitehead Institute for
969 Biomedical Research, Center for Genome Research:, Lander, E.S., Linton, L.M., Birren, B.,
970 Nusbaum, C., Zody, M.C., Baldwin, J., Devon, K., Dewar, K., et al. (2001). Initial sequencing
971 and analysis of the human genome. Nature *409*, 860–921. 10.1038/35057062.
972 2. Penzkofer, T., Jäger, M., Figlerowicz, M., Badge, R., Mundlos, S., Robinson, P.N.,
973 and Zemojtel, T. (2017). L1Base 2: more retrotransposition-active LINE-1s, more mammalian
974 genomes. Nucleic Acids Res *45*, D68–D73. 10.1093/nar/gkw925.
975 3. Gasior, S.L., Wakeman, T.P., Xu, B., and Deininger, P.L. (2006). The Human LINE-1
976 Retrotransposon Creates DNA Double-strand Breaks. Journal of Molecular Biology *357*,
977 1383–1393. 10.1016/j.jmb.2006.01.089.
978 4. Belgnaoui, S.M., Gosden, R.G., Semmes, O.J., and Haoudi, A. (2006). Human LINE-
979 1 retrotransposon induces DNA damage and apoptosis in cancer cells. Cancer Cell
980 International *6*, 13. 10.1186/1475-2867-6-13.
981 5. Blaudin de Thé, F., Rekaik, H., Peze-Heidsieck, E., Massiani-Beaudoin, O., Joshi,
982 R.L., Fuchs, J., and Prochiantz, A. (2018). Engrailed homeoprotein blocks degeneration in
983 adult dopaminergic neurons through LINE-1 repression. EMBO J *37*.
984 10.15252/embj.201797374.
985 6. Simon, M., Van Meter, M., Ablaeva, J., Ke, Z., Gonzalez, R.S., Taguchi, T., De
986 Cecco, M., Leonova, K.I., Kogan, V., Helfand, S.L., et al. (2019). LINE1 Derepression in
987 Aged Wild-Type and SIRT6-Deficient Mice Drives Inflammation. Cell Metabolism *29*, 871-
988 885.e5. 10.1016/j.cmet.2019.02.014.
989 7. Thomas, C.A., Tejwani, L., Trujillo, C.A., Negraes, P.D., Herai, R.H., Mesci, P.,
990 Macia, A., Crow, Y.J., and Muotri, A.R. (2017). Modeling of TREX1-Dependent
991 Autoimmune Disease using Human Stem Cells Highlights L1 Accumulation as a Source of
992 Neuroinflammation. Cell Stem Cell *21*, 319-331.e8. 10.1016/j.stem.2017.07.009.
993 8. De Cecco, M., Ito, T., Petrashen, A.P., Elias, A.E., Skvir, N.J., Criscione, S.W.,
994 Caligiana, A., Brocculi, G., Adney, E.M., Boeke, J.D., et al. (2019). Author Correction: L1
995 drives IFN in senescent cells and promotes age-associated inflammation. Nature *572*, E5–E5.
996 10.1038/s41586-019-1350-9.
997 9. Douville, R., Liu, J., Rothstein, J., and Nath, A. (2011). Identification of active loci of
998 a human endogenous retrovirus in neurons of patients with amyotrophic lateral sclerosis. Ann
999 Neurol. *69*, 141–151. 10.1002/ana.22149.
1000 10. Li, W., Jin, Y., Prazak, L., Hammell, M., and Dubnau, J. (2012). Transposable
1001 Elements in TDP-43-Mediated Neurodegenerative Disorders. PLoS ONE *7*, e44099.
1002 10.1371/journal.pone.0044099.
1003 11. Krug, L., Chatterjee, N., Borges-Monroy, R., Hearn, S., Liao, W.-W., Morrill, K.,
1004 Prazak, L., Rozhkov, N., Theodorou, D., Hammell, M., et al. (2017). Retrotransposon
1005 activation contributes to neurodegeneration in a Drosophila TDP-43 model of ALS. PLoS
1006 Genet *13*, e1006635. 10.1371/journal.pgen.1006635.
1007 12. Prudencio, M., Gonzales, P.K., Cook, C.N., Gendron, T.F., Daughrity, L.M., Song, Y.,
1008 Ebbert, M.T.W., van Blitterswijk, M., Zhang, Y.-J., Jansen-West, K., et al. (2017). Repetitive
1009 element transcripts are elevated in the brain of C9orf72 ALS/FTLD patients. Human
1010 Molecular Genetics *26*, 3421–3431. 10.1093/hmg/ddx233.
1011 13. Sun, W., Samimi, H., Gamez, M., Zare, H., and Frost, B. (2018). Pathogenic tau-
1012 induced piRNA depletion promotes neuronal death through transposable element
1013 dysregulation in neurodegenerative tauopathies. Nat Neurosci *21*, 1038–1048.

1014 10.1038/s41593-018-0194-1.
1015 14. Guo, C., Jeong, H.-H., Hsieh, Y.-C., Klein, H.-U., Bennett, D.A., De Jager, P.L., Liu,
1016 Z., and Shulman, J.M. (2018). Tau Activates Transposable Elements in Alzheimer's Disease.
1017 Cell Reports *23*, 2874–2880. 10.1016/j.celrep.2018.05.004.
1018 15. Gan, L., Cookson, M.R., Petrucelli, L., and La Spada, A.R. (2018). Converging
1019 pathways in neurodegeneration, from genetics to mechanisms. Nat Neurosci *21*, 1300–1309.
1020 10.1038/s41593-018-0237-7.
1021 16. Fu, H., Hardy, J., and Duff, K.E. (2018). Selective vulnerability in neurodegenerative
1022 diseases. Nat Neurosci *21*, 1350–1358. 10.1038/s41593-018-0221-2.
1023 17. Ravel-Godreuil, C., Massiani-Beaudoin, O., Mailly, P., Prochiantz, A., Joshi, R.L.,
1024 and Fuchs, J. (2021). Perturbed DNA methylation by Gadd45b induces chromatin
1025 disorganization, DNA strand breaks and dopaminergic neuron death. iScience *24*, 102756.
1026 10.1016/j.isci.2021.102756.
1027 18. Frost, B., Hemberg, M., Lewis, J., and Feany, M.B. (2014). Tau promotes
1028 neurodegeneration through global chromatin relaxation. Nat Neurosci *17*, 357–366.
1029 10.1038/nn.3639.
1030 19. Rekaik, H., Blaudin de Thé, F.-X., Fuchs, J., Massiani-Beaudoin, O., Prochiantz, A.,
1031 and Joshi, R.L. (2015). Engrailed Homeoprotein Protects Mesencephalic Dopaminergic
1032 Neurons from Oxidative Stress. Cell Reports *13*, 242–250. 10.1016/j.celrep.2015.08.076.
1033 20. Peze-Heidsieck, E., Bonnifet, T., Znaidi, R., Ravel-Godreuil, C., Massiani-Beaudoin,
1034 O., Joshi, R.L., and Fuchs, J. (2022). Retrotransposons as a Source of DNA Damage in
1035 Neurodegeneration. Frontiers in Aging Neuroscience *13*.
1036 21. Lotharius, J., Barg, S., Wiekop, P., Lundberg, C., Raymon, H.K., and Brundin, P.
1037 (2002). Effect of Mutant α-Synuclein on Dopamine Homeostasis in a New Human
1038 Mesencephalic Cell Line. Journal of Biological Chemistry *277*, 38884–38894.
1039 10.1074/jbc.M205518200.
1040 22. Lotharius, J., Falsig, J., Van Beek, J., Payne, S., Dringen, R., Brundin, P., and Leist,
1041 M. (2005). Progressive Degeneration of Human Mesencephalic Neuron-Derived Cells
1042 Triggered by Dopamine-Dependent Oxidative Stress Is Dependent on the Mixed-Lineage
1043 Kinase Pathway. J. Neurosci. *25*, 6329–6342. 10.1523/JNEUROSCI.1746-05.2005.
1044 23. Scholz, D., Pöltl, D., Genewsky, A., Weng, M., Waldmann, T., Schildknecht, S., and
1045 Leist, M. (2011). Rapid, complete and large-scale generation of post-mitotic neurons from the
1046 human LUHMES cell line: LUHMES as widely applicable neuronal model system. Journal of
1047 Neurochemistry *119*, 957–971. 10.1111/j.1471-4159.2011.07255.x.
1048 24. Schindelin, J., Arganda-Carreras, I., Frise, E., Kaynig, V., Longair, M., Pietzsch, T.,
1049 Preibisch, S., Rueden, C., Saalfeld, S., Schmid, B., et al. (2012). Fiji: an open-source platform
1050 for biological-image analysis. Nat Methods *9*, 676–682. 10.1038/nmeth.2019.
1051 25. Linkert, M., Rueden, C.T., Allan, C., Burel, J.-M., Moore, W., Patterson, A.,
1052 Loranger, B., Moore, J., Neves, C., MacDonald, D., et al. (2010). Metadata matters: access to
1053 image data in the real world. Journal of Cell Biology *189*, 777–782. 10.1083/jcb.201004104.
1054 26. Ollion, J., Cochennec, J., Loll, F., Escudé, C., and Boudier, T. (2013). TANGO: a
1055 generic tool for high-throughput 3D image analysis for studying nuclear organization.
1056 Bioinformatics *29*, 1840–1841. 10.1093/bioinformatics/btt276.
1057 27. Stringer, C., Wang, T., Michaelos, M., and Pachitariu, M. (2021). Cellpose: a
1058 generalist algorithm for cellular segmentation. Nature Methods *18*, 100–107.
1059 28. Schmidt, U., Weigert, M., Broaddus, C., and Myers, G. (2018). Cell Detection with
1060 Star-Convex Polygons. In Medical Image Computing and Computer Assisted Intervention –
1061 MICCAI 2018 Lecture Notes in Computer Science., A. F. Frangi, J. A. Schnabel, C.
1062 Davatzikos, C. Alberola-López, and G. Fichtinger, eds. (Springer International Publishing),
1063 pp. 265–273. 10.1007/978-3-030-00934-2_30.

1064 29. Haase, R., Royer, L.A., Steinbach, P., Schmidt, D., Dibrov, A., Schmidt, U., Weigert,
1065 M., Maghelli, N., Tomancak, P., Jug, F., et al. (2020). CLIJ: GPU-accelerated image
1066 processing for everyone. Nat Methods *17*, 5–6. 10.1038/s41592-019-0650-1.
1067 30. Pachitariu, M., and Stringer, C. (2022). Cellpose 2.0: how to train your own model.
1068 Nat Methods *19*, 1634–1641. 10.1038/s41592-022-01663-4.
1069 31. Zhang, X., Yin, M., and Zhang, M. (2014). Cell-based assays for Parkinson's disease
1070 using differentiated human LUHMES cells. Acta Pharmacol Sin *35*, 945–956.
1071 10.1038/aps.2014.36.
1072 32. Harris, G., Hogberg, H., Hartung, T., and Smirnova, L. (2017). 3D Differentiation of
1073 LUHMES Cell Line to Study Recovery and Delayed Neurotoxic Effects. Current Protocols in
1074 Toxicology *73*, 11.23.1-11.23.28. 10.1002/cptx.29.
1075 33. Harischandra, D.S., Rokad, D., Ghaisas, S., Verma, S., Robertson, A., Jin, H.,
1076 Anantharam, V., Kanthasamy, A., and Kanthasamy, A.G. (2020). Enhanced differentiation of
1077 human dopaminergic neuronal cell model for preclinical translational research in Parkinson's
1078 disease. Biochimica et Biophysica Acta (BBA) - Molecular Basis of Disease *1866*, 165533.
1079 10.1016/j.bbadis.2019.165533.
1080 34. Junqueira, V.B.C., Barros, S.B.M., Chan, S.S., Rodrigues, L., Giavarotti, L., Abud,
1081 R.L., and Deucher, G.P. (2004). Aging and oxidative stress. Molecular Aspects of Medicine
1082 *25*, 5–16. 10.1016/j.mam.2004.02.003.
1083 35. Romano, A.D., Serviddio, G., de Matthaeis, A., Bellanti, F., and Vendemiale, G.
1084 (2010). Oxidative stress and aging. J Nephrol *23 Suppl 15*, S29-36.
1085 36. Liguori, I., Russo, G., Curcio, F., Bulli, G., Aran, L., Della-Morte, D., Gargiulo, G.,
1086 Testa, G., Cacciatore, F., Bonaduce, D., et al. (2018). Oxidative stress, aging, and diseases.
1087 CIA *Volume 13*, 757–772. 10.2147/CIA.S158513.
1088 37. Hayes, J.D., Dinkova-Kostova, A.T., and Tew, K.D. (2020). Oxidative Stress in
1089 Cancer. Cancer Cell *38*, 167–197. 10.1016/j.ccell.2020.06.001.
1090 38. Emerit, J., Edeas, M., and Bricaire, F. (2004). Neurodegenerative diseases and
1091 oxidative stress. Biomedicine & Pharmacotherapy *58*, 39–46. 10.1016/j.biopha.2003.11.004.
1092 39. Chen, X., Guo, C., and Kong, J. (2012). Oxidative stress in neurodegenerative
1093 diseases. Neural Regen Res *7*, 376–385. 10.3969/j.issn.1673-5374.2012.05.009.
1094 40. Kim, G.H., Kim, J.E., Rhie, S.J., and Yoon, S. (2015). The Role of Oxidative Stress in
1095 Neurodegenerative Diseases. Exp Neurobiol *24*, 325–340. 10.5607/en.2015.24.4.325.
1096 41. Fischer, R., and Maier, O. (2015). Interrelation of Oxidative Stress and Inflammation
1097 in Neurodegenerative Disease: Role of TNF. Oxidative Medicine and Cellular Longevity
1098 *2015*, e610813. 10.1155/2015/610813.
1099 42. Giorgi, G., Marcantonio, P., and Del Re, B. (2011). LINE-1 retrotransposition in
1100 human neuroblastoma cells is affected by oxidative stress. Cell Tissue Res *346*, 383–391.
1101 10.1007/s00441-011-1289-0.
1102 43. Wongpaiboonwattana, W., Tosukhowong, P., Dissayabutra, T., Mutirangura, A., and
1103 Boonla, C. (2013). Oxidative Stress Induces Hypomethylation of LINE-1 and
1104 Hypermethylation of the RUNX3 Promoter in a Bladder Cancer Cell Line. Asian Pacific
1105 Journal of Cancer Prevention *14*, 3773–3778. 10.7314/APJCP.2013.14.6.3773.
1106 44. Whongsiri, P., Pimratana, C., Wijitsettakul, U., Sanpavat, A., Jindatip, D., Hoffmann,
1107 M.J., Goering, W., Schulz, W.A., and Boonla, C. (2019). Oxidative stress and LINE-1
1108 reactivation in bladder cancer are epigenetically linked through active chromatin formation.
1109 Free Radical Biology and Medicine *134*, 419–428. 10.1016/j.freeradbiomed.2019.01.031.
1110 45. Thomas, C.A., Tejwani, L., Trujillo, C.A., Negraes, P.D., Herai, R.H., Mesci, P.,
1111 Macia, A., Crow, Y.J., and Muotri, A.R. (2017). Modeling of TREX1-Dependent
1112 Autoimmune Disease using Human Stem Cells Highlights L1 Accumulation as a Source of
1113 Neuroinflammation. Cell Stem Cell *21*, 319-331.e8. 10.1016/j.stem.2017.07.009.

1114 46. Mita, P., Wudzinska, A., Sun, X., Andrade, J., Nayak, S., Kahler, D.J., Badri, S.,
1115 LaCava, J., Ueberheide, B., Yun, C.Y., et al. (2018). LINE-1 protein localization and
1116 functional dynamics during the cell cycle. eLife *7*, e30058. 10.7554/eLife.30058.
1117 47. Freeman, B.T., Sokolowski, M., Roy-Engel, A.M., Smither, M.E., and Belancio, V.P.
1118 (2019). Identification of charged amino acids required for nuclear localization of human L1
1119 ORF1 protein. Mobile DNA *10*, 20. 10.1186/s13100-019-0159-2.
1120 48. Idica, A., Sevrioukov, E.A., Zisoulis, D.G., Hamdorf, M., Daugaard, I., Kadandale, P.,
1121 and Pedersen, I.M. (2017). MicroRNA miR-128 represses LINE-1 (L1) retrotransposition by
1122 down-regulating the nuclear import factor TNPO1. Journal of Biological Chemistry *292*,
1123 20494–20508. 10.1074/jbc.M117.807677.
1124 49. Walther, T.C., Fornerod, M., Pickersgill, H., Goldberg, M., Allen, T.D., and Mattaj,
1125 I.W. (2001). The nucleoporin Nup153 is required for nuclear pore basket formation, nuclear
1126 pore complex anchoring and import of a subset of nuclear proteins. The EMBO Journal *20*,
1127 5703–5714. 10.1093/emboj/20.20.5703.
1128 50. Kapinos, L.E., Huang, B., Rencurel, C., and Lim, R.Y.H. (2017). Karyopherins
1129 regulate nuclear pore complex barrier and transport function. Journal of Cell Biology *216*,
1130 3609–3624. 10.1083/jcb.201702092.
1131 51. Hirsch, E., Graybiel, A.M., and Agid, Y.A. (1988). Melanized dopaminergic neurons
1132 are differentially susceptible to degeneration in Parkinson's disease. Nature *334*, 345–348.
1133 10.1038/334345a0.
1134 52. Liu, S., Sawada, T., Lee, S., Yu, W., Silverio, G., Alapatt, P., Millan, I., Shen, A.,
1135 Saxton, W., Kanao, T., et al. (2012). Parkinson's Disease–Associated Kinase PINK1
1136 Regulates Miro Protein Level and Axonal Transport of Mitochondria. PLoS Genet *8*,
1137 e1002537. 10.1371/journal.pgen.1002537.
1138 53. Bird, S.L., Heald, R., and Weis, K. (2013). RanGTP and CLASP1 cooperate to
1139 position the mitotic spindle. MBoC *24*, 2506–2514. 10.1091/mbc.e13-03-0150.
1140 54. Soderholm, J.F., Bird, S.L., Kalab, P., Sampathkumar, Y., Hasegawa, K., Uehara-
1141 Bingen, M., Weis, K., and Heald, R. (2011). Importazole, a Small Molecule Inhibitor of the
1142 Transport Receptor Importin-β. ACS Chem. Biol. *6*, 700–708. 10.1021/cb2000296.
1143 55. Wagstaff, K.M., Sivakumaran, H., Heaton, S.M., Harrich, D., and Jans, D.A. (2012).
1144 Ivermectin is a specific inhibitor of importin α/β-mediated nuclear import able to inhibit
1145 replication of HIV-1 and dengue virus. Biochemical Journal *443*, 851–856.
1146 10.1042/BJ20120150.
1147 56. Yang, S.N.Y., Atkinson, S.C., Wang, C., Lee, A., Bogoyevitch, M.A., Borg, N.A., and
1148 Jans, D.A. (2020). The broad spectrum antiviral ivermectin targets the host nuclear transport
1149 importin α/β1 heterodimer. Antiviral Research *177*, 104760. 10.1016/j.antiviral.2020.104760.
1150 57. Ren, W., Fan, H., Grimm, S.A., Kim, J.J., Li, L., Guo, Y., Petell, C.J., Tan, X.-F.,
1151 Zhang, Z.-M., Coan, J.P., et al. (2021). DNMT1 reads heterochromatic H4K20me3 to
1152 reinforce LINE-1 DNA methylation. Nat Commun *12*, 2490. 10.1038/s41467-021-22665-4.
1153 58. Zhang, K., Donnelly, C.J., Haeusler, A.R., Grima, J.C., Machamer, J.B., Steinwald, P.,
1154 Daley, E.L., Miller, S.J., Cunningham, K.M., Vidensky, S., et al. (2015). The C9orf72 repeat
1155 expansion disrupts nucleocytoplasmic transport. Nature *525*, 56–61. 10.1038/nature14973.
1156 59. Gao, J., Wang, L., Huntley, M.L., Perry, G., and Wang, X. (2018). Pathomechanisms
1157 of TDP-43 in neurodegeneration. Journal of Neurochemistry *146*, 7–20. 10.1111/jnc.14327.
1158 60. Lee, S.M., Asress, S., Hales, C.M., Gearing, M., Vizcarra, J.C., Fournier, C.N.,
1159 Gutman, D.A., Chin, L.-S., Li, L., and Glass, J.D. (2019). TDP-43 cytoplasmic inclusion
1160 formation is disrupted in C9orf72-associated amyotrophic lateral sclerosis/frontotemporal
1161 lobar degeneration. Brain Communications *1*, fcz014. 10.1093/braincomms/fcz014.
1162 61. Neumann, M., Sampathu, D.M., Kwong, L.K., Truax, A.C., Micsenyi, M.C., Chou,
1163 T.T., Bruce, J., Schuck, T., Grossman, M., Clark, C.M., et al. (2006). Ubiquitinated TDP-43

1164 in Frontotemporal Lobar Degeneration and Amyotrophic Lateral Sclerosis. Science *314*, 130–
1165 133. 10.1126/science.1134108.
1166 62. Aizawa, H., Yamashita, T., Kato, H., Kimura, T., and Kwak, S. (2019). Impaired
1167 Nucleoporins Are Present in Sporadic Amyotrophic Lateral Sclerosis Motor Neurons that
1168 Exhibit Mislocalization of the 43-kDa TAR DNA-Binding Protein. J Clin Neurol *15*, 62.
1169 10.3988/jcn.2019.15.1.62.
1170 63. Chou, C.-C., Zhang, Y., Umoh, M.E., Vaughan, S.W., Lorenzini, I., Liu, F., Sayegh,
1171 M., Donlin-Asp, P.G., Chen, Y.H., Duong, D.M., et al. (2018). TDP-43 pathology disrupts
1172 nuclear pore complexes and nucleocytoplasmic transport in ALS/FTD. Nat Neurosci *21*, 228–
1173 239. 10.1038/s41593-017-0047-3.
1174 64. Lin, Y.-C., Kumar, M.S., Ramesh, N., Anderson, E.N., Nguyen, A.T., Kim, B.,
1175 Cheung, S., McDonough, J.A., Skarnes, W.C., Lopez-Gonzalez, R., et al. (2021). Interactions
1176 between ALS-linked FUS and nucleoporins are associated with defects in the
1177 nucleocytoplasmic transport pathway. Nat Neurosci *24*, 1077–1088. 10.1038/s41593-021-
1178 00859-9.
1179 65. Scaffidi, P., and Misteli, T. (2006). Lamin A-Dependent Nuclear Defects in Human
1180 Aging. Science *312*, 1059–1063. 10.1126/science.1127168.
1181 66. Worman, H.J. (2012). Nuclear lamins and laminopathies. The Journal of Pathology
1182 *226*, 316–325. 10.1002/path.2999.
1183 67. Stiekema, M., van Zandvoort, M.A.M.J., Ramaekers, F.C.S., and Broers, J.L.V.
1184 (2020). Structural and Mechanical Aberrations of the Nuclear Lamina in Disease. Cells *9*,
1185 1884. 10.3390/cells9081884.
1186 68. De Sandre-Giovannoli, A., Bernard, R., Cau, P., Navarro, C., Amiel, J., Boccaccio, I.,
1187 Lyonnet, S., Stewart, C.L., Munnich, A., Le Merrer, M., et al. (2003). Lamin A Truncation in
1188 Hutchinson-Gilford Progeria. Science *300*, 2055–2055. 10.1126/science.1084125.
1189 69. Larrieu, D., Viré, E., Robson, S., Breusegem, S.Y., Kouzarides, T., and Jackson, S.P.
1190 (2018). Inhibition of the acetyltransferase NAT10 normalizes progeric and aging cells by
1191 rebalancing the Transportin-1 nuclear import pathway. Science Signaling *11*, eaar5401.
1192 10.1126/scisignal.aar5401.
1193 70. Larrieu, D., Britton, S., Demir, M., Rodriguez, R., and Jackson, S.P. (2014). Chemical
1194 Inhibition of NAT10 Corrects Defects of Laminopathic Cells. Science *344*, 527–532.
1195 10.1126/science.1252651.
1196 71. Rangasamy, D. (2013). Distinctive patterns of epigenetic marks are associated with
1197 promoter regions of mouse LINE-1 and LTR retrotransposons. Mobile DNA *4*, 27.
1198 10.1186/1759-8753-4-27.
1199 72. Casale, A.M., Liguori, F., Ansaloni, F., Cappucci, U., Finaurini, S., Spirito, G.,
1200 Persichetti, F., Sanges, R., Gustincich, S., and Piacentini, L. (2021). Transposable element
1201 activation promotes neurodegeneration in a Drosophila model of Huntington's disease.
1202 iScience *25*, 103702. 10.1016/j.isci.2021.103702.
1203 73. Tam, O.H., Rozhkov, N.V., Shaw, R., Kim, D., Hubbard, I., Fennessey, S., Propp, N.,
1204 Fagegaltier, D., Harris, B.T., Ostrow, L.W., et al. (2019). Postmortem Cortex Samples
1205 Identify Distinct Molecular Subtypes of ALS: Retrotransposon Activation, Oxidative Stress,
1206 and Activated Glia. Cell Reports *29*, 1164-1177.e5. 10.1016/j.celrep.2019.09.066.
1207 74. Ravel-Godreuil, C., Znaidi, R., Bonnifet, T., Joshi, R.L., and Fuchs, J. (2021).
1208 Transposable elements as new players in neurodegenerative diseases. FEBS Letters *595*,
1209 2733–2755. 10.1002/1873-3468.14205.
1210 75. Dai, L., LaCava, J., Taylor, M.S., and Boeke, J.D. (2014). Expression and detection of
1211 LINE-1 ORF-encoded proteins. Mobile Genetic Elements. 10.4161/mge.29319.
1212 76. Rangasamy, D., Lenka, N., Ohms, S., Dahlstrom, J.E., Blackburn, A.C., and Board,
1213 P.G. (2015). Activation of LINE-1 Retrotransposon Increases the Risk of Epithelial-

1214 Mesenchymal Transition and Metastasis in Epithelial Cancer. Current Molecular Medicine
1215 *15*, 588–597.
1216 77. Macia, A., Widmann, T.J., Heras, S.R., Ayllon, V., Sanchez, L., Benkaddour-
1217 Boumzaouad, M., Muñoz-Lopez, M., Rubio, A., Amador-Cubero, S., Blanco-Jimenez, E., et
1218 al. (2017). Engineered LINE-1 retrotransposition in nondividing human neurons. Genome
1219 Res. *27*, 335–348. 10.1101/gr.206805.116.
1220 78. Sur, D., Kustwar, R.K., Budania, S., Mahadevan, A., Hancks, D.C., Yadav, V.,
1221 Shankar, S.K., and Mandal, P.K. (2017). Detection of the LINE-1 retrotransposon RNA-
1222 binding protein ORF1p in different anatomical regions of the human brain. Mobile DNA *8*,
1223 17. 10.1186/s13100-017-0101-4.
1224 79. Pereira, G.C., Sanchez, L., Schaughency, P.M., Rubio-Roldán, A., Choi, J.A., Planet,
1225 E., Batra, R., Turelli, P., Trono, D., Ostrow, L.W., et al. (2018). Properties of LINE-1 proteins
1226 and repeat element expression in the context of amyotrophic lateral sclerosis. Mobile DNA *9*,
1227 35. 10.1186/s13100-018-0138-z.
1228 80. Twyffels, L., Gueydan, C., and Kruys, V. (2014). Transportin-1 and Transportin-2:
1229 Protein nuclear import and beyond. FEBS Letters *588*, 1857–1868.
1230 10.1016/j.febslet.2014.04.023.
1231 81. Kimura, M., Okumura, N., Kose, S., Takao, T., and Imamoto, N. (2013). Identification
1232 of Cargo Proteins Specific for Importin-β with Importin-α Applying a Stable Isotope Labeling
1233 by Amino Acids in Cell Culture (SILAC)-based in Vitro Transport System *. Journal of
1234 Biological Chemistry *288*, 24540–24549. 10.1074/jbc.M113.489286.
1235 82. Manhas, S., Ma, L., and Measday, V. (2018). The yeast Ty1 retrotransposon requires
1236 components of the nuclear pore complex for transcription and genomic integration. Nucleic
1237 Acids Research *46*, 3552–3578. 10.1093/nar/gky109.
1238 83. Candia, R.F., Cohen, L.S., Morozova, V., Corbo, C., and Alonso, A.D. (2022).
1239 Importin-Mediated Pathological Tau Nuclear Translocation Causes Disruption of the Nuclear
1240 Lamina, TDP-43 Mislocalization and Cell Death. Frontiers in Molecular Neuroscience *15*.
1241 84. Arora, R., Bodak, M., Penouty, L., Hackman, C., and Ciaudo, C. (2022). Sequestration
1242 of LINE -1 in cytosolic aggregates by MOV10 restricts retrotransposition. EMBO Reports *23*,
1243 e54458. 10.15252/embr.202154458.
1244 85. Briggs, E.M., McKerrow, W., Mita, P., Boeke, J.D., Logan, S.K., and Fenyö, D.
1245 (2021). RIP-seq reveals LINE-1 ORF1p association with p-body enriched mRNAs. Mob
1246 DNA *12*, 5. 10.1186/s13100-021-00233-3.
1247 86. Paonessa, F., Evans, L.D., Solanki, R., Larrieu, D., Wray, S., Hardy, J., Jackson, S.P.,
1248 and Livesey, F.J. (2019). Microtubules Deform the Nuclear Membrane and Disrupt
1249 Nucleocytoplasmic Transport in Tau-Mediated Frontotemporal Dementia. Cell Reports *26*,
1250 582-593.e5. 10.1016/j.celrep.2018.12.085.
1251 87. Kim, H.J., and Taylor, J.P. (2017). Lost in Transportation: Nucleocytoplasmic
1252 Transport Defects in ALS and Other Neurodegenerative Diseases. Neuron *96*, 285–297.
1253 10.1016/j.neuron.2017.07.029.
1254 88. Kinoshita, Y., Ito, H., Hirano, A., Fujita, K., Wate, R., Nakamura, M., Kaneko, S.,
1255 Nakano, S., and Kusaka, H. (2009). Nuclear Contour Irregularity and Abnormal Transporter
1256 Protein Distribution in Anterior Horn Cells in Amyotrophic Lateral Sclerosis. Journal of
1257 Neuropathology & Experimental Neurology *68*, 1184–1192.
1258 10.1097/NEN.0b013e3181bc3bec.
1259 89. Sheffield, L.G., Miskiewicz, H.B., Tannenbaum, L.B., and Mirra, S.S. (2006). Nuclear
1260 Pore Complex Proteins in Alzheimer Disease. Journal of Neuropathology & Experimental
1261 Neurology *65*, 45–54. 10.1097/01.jnen.0000195939.40410.08.
1262 90. Gasset-Rosa, F., Chillon-Marinas, C., Goginashvili, A., Atwal, R.S., Artates, J.W.,
1263 Tabet, R., Wheeler, V.C., Bang, A.G., Cleveland, D.W., and Lagier-Tourenne, C. (2017).

1264 Polyglutamine-Expanded Huntingtin Exacerbates Age-Related Disruption of Nuclear
1265 Integrity and Nucleocytoplasmic Transport. Neuron *94*, 48-57.e4.
1266 10.1016/j.neuron.2017.03.027.
1267 91. Grima, J.C., Daigle, J.G., Arbez, N., Cunningham, K.C., Zhang, K., Ochaba, J.,
1268 Geater, C., Morozko, E., Stocksdale, J., Glatzer, J.C., et al. (2017). Mutant Huntingtin
1269 Disrupts the Nuclear Pore Complex. Neuron *94*, 93-107.e6. 10.1016/j.neuron.2017.03.023.
1270 92. Guo, L., Fare, C.M., and Shorter, J. (2019). Therapeutic Dissolution of Aberrant
1271 Phases by Nuclear-Import Receptors. Trends in Cell Biology *29*, 308–322.
1272 10.1016/j.tcb.2018.12.004.
1273 93. Savas, J.N., Toyama, B.H., Xu, T., Yates, J.R., and Hetzer, M.W. (2012). Extremely
1274 Long-Lived Nuclear Pore Proteins in the Rat Brain. Science *335*, 942–942.
1275 10.1126/science.1217421.
1276 94. Toyama, B.H., Savas, J.N., Park, S.K., Harris, M.S., Ingolia, N.T., Yates, J.R., and
1277 Hetzer, M.W. (2013). Identification of Long-Lived Proteins Reveals Exceptional Stability of
1278 Essential Cellular Structures. Cell *154*, 971–982. 10.1016/j.cell.2013.07.037.
1279 95. D'Angelo, M.A., Raices, M., Panowski, S.H., and Hetzer, M.W. (2009). Age-
1280 Dependent Deterioration of Nuclear Pore Complexes Causes a Loss of Nuclear Integrity in
1281 Postmitotic Cells. Cell *136*, 284–295. 10.1016/j.cell.2008.11.037.
1282 96. Hetzer, M.W. (2010). The Nuclear Envelope. Cold Spring Harbor Perspectives in
1283 Biology *2*, a000539–a000539. 10.1101/cshperspect.a000539.
1284 97. Eftekharzadeh, B., Daigle, J.G., Kapinos, L.E., Coyne, A., Schiantarelli, J.,
1285 Carlomagno, Y., Cook, C., Miller, S.J., Dujardin, S., Amaral, A.S., et al. (2018). Tau Protein
1286 Disrupts Nucleocytoplasmic Transport in Alzheimer's Disease. Neuron *99*, 925-940.e7.
1287 10.1016/j.neuron.2018.07.039.
1288 98. Buratti, E., and Baralle, F.E. (2010). The multiple roles of TDP-43 in pre-mRNA
1289 processing and gene expression regulation. RNA Biology *7*, 420–429. 10.4161/rna.7.4.12205.
1290 99. Colombrita, C., Onesto, E., Megiorni, F., Pizzuti, A., Baralle, F.E., Buratti, E., Silani,
1291 V., and Ratti, A. (2012). TDP-43 and FUS RNA-binding Proteins Bind Distinct Sets of
1292 Cytoplasmic Messenger RNAs and Differently Regulate Their Post-transcriptional Fate in
1293 Motoneuron-like Cells. Journal of Biological Chemistry *287*, 15635–15647.
1294 10.1074/jbc.M111.333450.
1295 100. Barmada, S.J., Skibinski, G., Korb, E., Rao, E.J., Wu, J.Y., and Finkbeiner, S. (2010).
1296 Cytoplasmic Mislocalization of TDP-43 Is Toxic to Neurons and Enhanced by a Mutation
1297 Associated with Familial Amyotrophic Lateral Sclerosis. J. Neurosci. *30*, 639–649.
1298 10.1523/JNEUROSCI.4988-09.2010.
1299 101. Benajiba, L., Le Ber, I., Camuzat, A., Lacoste, M., Thomas-Anterion, C., Couratier,
1300 P., Legallic, S., Salachas, F., Hannequin, D., Decousus, M., et al. (2009). TARDBP mutations
1301 in motoneuron disease with frontotemporal lobar degeneration. Annals of Neurology *65*, 470–
1302 473. 10.1002/ana.21612.
1303 102. Kabashi, E., Valdmanis, P.N., Dion, P., Spiegelman, D., McConkey, B.J., Velde, C.V.,
1304 Bouchard, J.-P., Lacomblez, L., Pochigaeva, K., Salachas, F., et al. (2008). TARDBP
1305 mutations in individuals with sporadic and familial amyotrophic lateral sclerosis. Nat Genet
1306 *40*, 572–574. 10.1038/ng.132.
1307 103. Sreedharan, J., Blair, I.P., Tripathi, V.B., Hu, X., Vance, C., Rogelj, B., Ackerley, S.,
1308 Durnall, J.C., Williams, K.L., Buratti, E., et al. (2008). TDP-43 Mutations in Familial and
1309 Sporadic Amyotrophic Lateral Sclerosis. Science *319*, 1668–1672. 10.1126/science.1154584.
1310 104. Duan, L., Zaepfel, B.L., Aksenova, V., Dasso, M., Rothstein, J.D., Kalab, P., and
1311 Hayes, L.R. (2022). Nuclear RNA binding regulates TDP-43 nuclear localization and passive
1312 nuclear export. Cell Reports *40*, 111106. 10.1016/j.celrep.2022.111106.
1313 105. Winton, M.J., Igaz, L.M., Wong, M.M., Kwong, L.K., Trojanowski, J.Q., and Lee,

V.M.-Y. (2008). Disturbance of Nuclear and Cytoplasmic TAR DNA-binding Protein (TDP-43) Induces Disease-like Redistribution, Sequestration, and Aggregate Formation *. Journal of Biological Chemistry *283*, 13302–13309. 10.1074/jbc.M800342200.

106. Ederle, H., and Dormann, D. (2017). TDP-43 and FUS *en route* from the nucleus to the cytoplasm. FEBS Lett *591*, 1489–1507. 10.1002/1873-3468.12646.

107. Frost, B. (2016). Alzheimer's disease: An acquired neurodegenerative laminopathy. Nucleus *7*, 275–283. 10.1080/19491034.2016.1183859.

108. Prissette, M., Fury, W., Koss, M., Racioppi, C., Fedorova, D., Dragileva, E., Clarke, G., Pohl, T., Dugan, J., Ahrens, D., et al. (2022). Disruption of nuclear envelope integrity as a possible initiating event in tauopathies. Cell Reports *40*, 111249. 10.1016/j.celrep.2022.111249.

109. Jiang, L., and Wolozin, B. (2021). Oligomeric tau disrupts nuclear envelope via binding to lamin proteins and lamin B receptor. Alzheimer's & Dementia *17*, e054521. 10.1002/alz.054521.

110. Martins, F., Sousa, J., Pereira, C.D., da Cruz e Silva, O.A.B., and Rebelo, S. (2020). Nuclear envelope dysfunction and its contribution to the aging process. Aging Cell *19*, e13143. 10.1111/acel.13143.

111. Mertens, J., Paquola, A.C.M., Ku, M., Hatch, E., Böhnke, L., Ladjevardi, S., McGrath, S., Campbell, B., Lee, H., Herdy, J.R., et al. (2015). Directly Reprogrammed Human Neurons Retain Aging-Associated Transcriptomic Signatures and Reveal Age-Related Nucleocytoplasmic Defects. Cell Stem Cell *17*, 705–718. 10.1016/j.stem.2015.09.001.

112. Oberdoerffer, P., and Sinclair, D.A. (2007). The role of nuclear architecture in genomic instability and ageing. Nat Rev Mol Cell Biol *8*, 692–702. 10.1038/nrm2238.

113. Jovičić, A., Mertens, J., Boeynaems, S., Bogaert, E., Chai, N., Yamada, S.B., Paul, J.W., Sun, S., Herdy, J.R., Bieri, G., et al. (2015). Modifiers of C9orf72 dipeptide repeat toxicity connect nucleocytoplasmic transport defects to FTD/ALS. Nat Neurosci *18*, 1226–1229. 10.1038/nn.4085.

114. Chang, L., Li, M., Shao, S., Li, C., Ai, S., Xue, B., Hou, Y., Zhang, Y., Li, R., Fan, X., et al. (2022). Nuclear peripheral chromatin-lamin B1 interaction is required for global integrity of chromatin architecture and dynamics in human cells. Protein & Cell *13*, 258–280. 10.1007/s13238-020-00794-8.

115. Perovanovic, J., Dell'Orso, S., Gnochi, V.F., Jaiswal, J.K., Sartorelli, V., Vigouroux, C., Mamchaoui, K., Mouly, V., Bonne, G., and Hoffman, E.P. (2016). Laminopathies disrupt epigenomic developmental programs and cell fate. Sci. Transl. Med. *8*. 10.1126/scitranslmed.aad4991.

116. Traxler, L., Lucciola, R., Herdy, J.R., Jones, J.R., Mertens, J., and Gage, F.H. (2023). Neural cell state shifts and fate loss in ageing and age-related diseases. Nat Rev Neurol *19*, 434–443. 10.1038/s41582-023-00815-0.

117. Richards, E.J., and Elgin, S.C.R. (2002). Epigenetic Codes for Heterochromatin Formation and Silencing. Cell *108*, 489–500. 10.1016/S0092-8674(02)00644-X.

118. Black, J.C., Van Rechem, C., and Whetstine, J.R. (2012). Histone Lysine Methylation Dynamics: Establishment, Regulation, and Biological Impact. Molecular Cell *48*, 491–507. 10.1016/j.molcel.2012.11.006.

119. Denais, C.M., Gilbert, R.M., Isermann, P., McGregor, A.L., Te Lindert, M., Weigelin, B., Davidson, P.M., Friedl, P., Wolf, K., and Lammerding, J. (2016). Nuclear envelope rupture and repair during cancer cell migration. Science *352*, 353–358. 10.1126/science.aad7297.

120. Nava, M.M., Miroshnikova, Y.A., Biggs, L.C., Whitefield, D.B., Metge, F., Boucas, J., Vihinen, H., Jokitalo, E., Li, X., García Arcos, J.M., et al. (2020). Heterochromatin-Driven Nuclear Softening Protects the Genome against Mechanical Stress-Induced Damage. Cell

*181*, 800-817.e22. 10.1016/j.cell.2020.03.052.
121. Raab, M., Gentili, M., De Belly, H., Thiam, H.-R., Vargas, P., Jimenez, A.J., Lautenschlaeger, F., Voituriez, R., Lennon-Duménil, A.-M., Manel, N., et al. (2016). ESCRT III repairs nuclear envelope ruptures during cell migration to limit DNA damage and cell death. Science *352*, 359–362. 10.1126/science.aad7611.
122. Hochmair, J., Exner, C., Franck, M., Dominguez-Baquero, A., Diez, L., Brognaro, H., Kraushar, M., Mielke, T., Radbruch, H., Kaniyappan, S., et al. (2022). Biomolecular Tau condensation is linked to Tau accumulation at the nuclear envelope. Preprint at bioRxiv, 10.1101/2022.01.24.477544 10.1101/2022.01.24.477544.
123. Gasset-Rosa, F., Lu, S., Yu, H., Chen, C., Melamed, Z., Guo, L., Shorter, J., Da Cruz, S., and Cleveland, D.W. (2019). Cytoplasmic TDP-43 De-mixing Independent of Stress Granules Drives Inhibition of Nuclear Import, Loss of Nuclear TDP-43, and Cell Death. Neuron *102*, 339-357.e7. 10.1016/j.neuron.2019.02.038.
124. Sil, S. (2022). Condensation of LINE-1 Is Required for Retrotransposition.
125. Shpyleva, S., Melnyk, S., Pavliv, O., Pogribny, I., and Jill James, S. (2018). Overexpression of LINE-1 Retrotransposons in Autism Brain. Mol Neurobiol *55*, 1740–1749. 10.1007/s12035-017-0421-x.
126. Bundo, M., Toyoshima, M., Okada, Y., Akamatsu, W., Ueda, J., Nemoto-Miyauchi, T., Sunaga, F., Toritsuka, M., Ikawa, D., Kakita, A., et al. (2014). Increased L1 Retrotransposition in the Neuronal Genome in Schizophrenia. Neuron *81*, 306–313. 10.1016/j.neuron.2013.10.053.
127. Doyle, G.A., Crist, R.C., Karatas, E.T., Hammond, M.J., Ewing, A.D., Ferraro, T.N., Hahn, C.-G., and Berrettini, W.H. (2017). Analysis of LINE-1 Elements in DNA from Postmortem Brains of Individuals with Schizophrenia. Neuropsychopharmacol. *42*, 2602–2611. 10.1038/npp.2017.115.
128. Liu, S., Du, T., Liu, Z., Shen, Y., Xiu, J., and Xu, Q. (2016). Inverse changes in L1 retrotransposons between blood and brain in major depressive disorder. Sci Rep *6*, 37530. 10.1038/srep37530.
129. Muotri, A.R., Marchetto, M.C.N., Coufal, N.G., Oefner, R., Yeo, G., Nakashima, K., and Gage, F.H. (2010). L1 retrotransposition in neurons is modulated by MeCP2. Nature *468*, 443–446. 10.1038/nature09544.
130. Zhao, B., Wu, Q., Ye, A.Y., Guo, J., Zheng, X., Yang, X., Yan, L., Liu, Q.-R., Hyde, T.M., Wei, L., et al. (2019). Somatic LINE-1 retrotransposition in cortical neurons and non-brain tissues of Rett patients and healthy individuals. PLOS Genetics *15*, e1008043. 10.1371/journal.pgen.1008043.
131. Coufal, N.G., Garcia-Perez, J.L., Peng, G.E., Marchetto, M.C.N., Muotri, A.R., Mu, Y., Carson, C.T., Macia, A., Moran, J.V., and Gage, F.H. (2011). Ataxia telangiectasia mutated (ATM) modulates long interspersed element-1 (L1) retrotransposition in human neural stem cells. Proceedings of the National Academy of Sciences *108*, 20382–20387. 10.1073/pnas.1100273108.
132. Van Eersel, J., Ke, Y.D., Gladbach, A., Bi, M., Götz, J., Kril, J.J., and Ittner, L.M. (2011). Cytoplasmic Accumulation and Aggregation of TDP-43 upon Proteasome Inhibition in Cultured Neurons. PLoS ONE *6*, e22850. 10.1371/journal.pone.0022850.
133. Della Valle, F., Thimma, M.P., Caiazzo, M., Pulcrano, S., Celii, M., Adroub, S.A., Liu, P., Alanis-Lobato, G., Broccoli, V., and Orlando, V. (2020). Transdifferentiation of Mouse Embryonic Fibroblasts into Dopaminergic Neurons Reactivates LINE-1 Repetitive Elements. Stem Cell Reports *14*, 60–74. 10.1016/j.stemcr.2019.12.002.

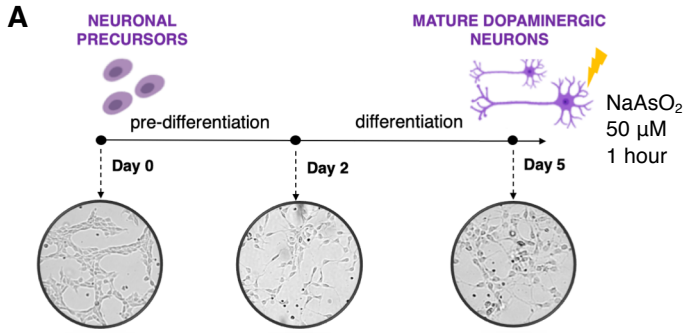
A
NEURONAL PRECURSORS
MATURE DOPAMINERGIC NEURONS
pre-differentiation
differentiation
Day 0
Day 2
Day 5
NaAsO2
50 µM
1 hour

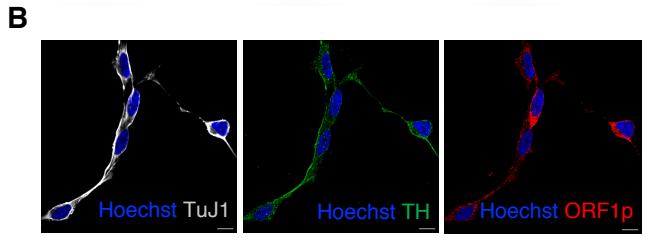
B
Hoechst TuJ1
Hoechst TH
Hoechst ORF1p

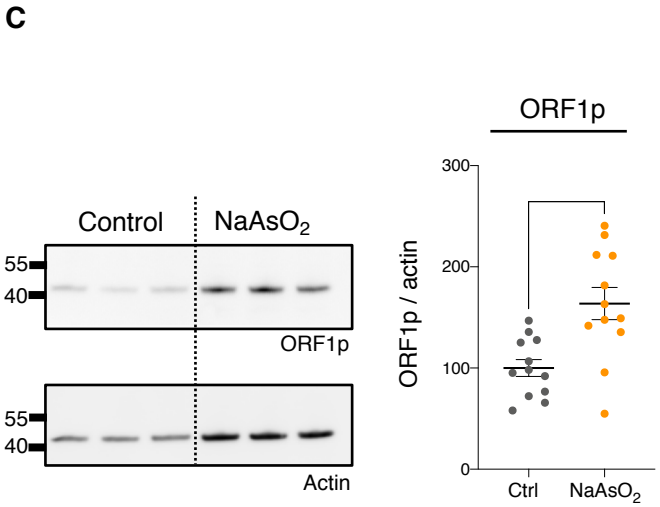
C
Control
NaAsO2
55
40
ORF1p
55
40
Actin
ORF1p
ORF1p / actin
300
200
100
0
Ctrl
NaAsO2

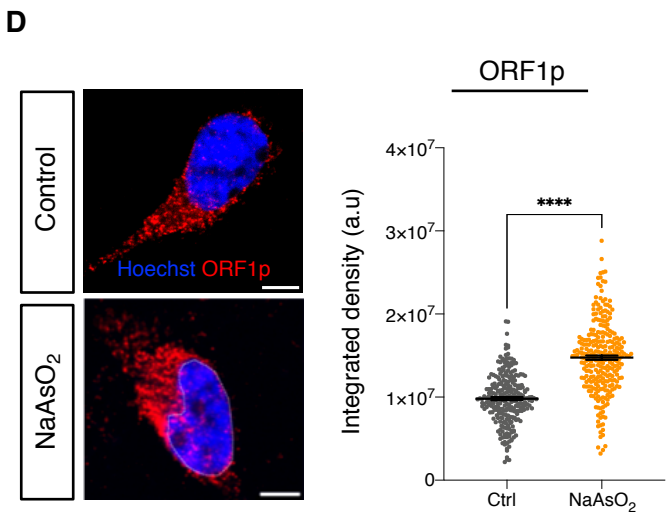
D
Control
NaAsO2
Hoechst ORF1p
ORF1p
Integrated density (a.u)
4x10^7
3x10^7
2x10^7
1x10^7
0
****
Ctrl
NaAsO2

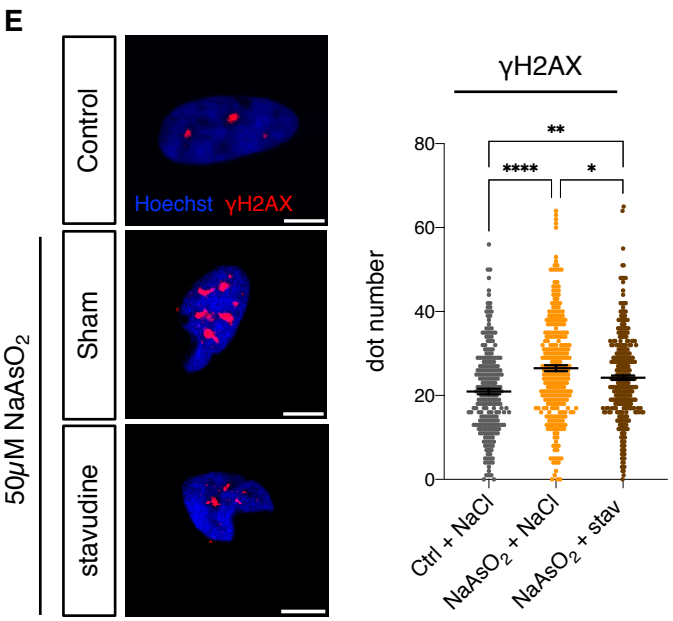
E
Control
Sham
stavudine
50µM NaAsO2
Hoechst γH2AX
γH2AX
dot number
80
60
40
20
0
**
****
*
Ctrl + NaCl
NaAsO2 + NaCl
NaAsO2 + stav

Fig. 1

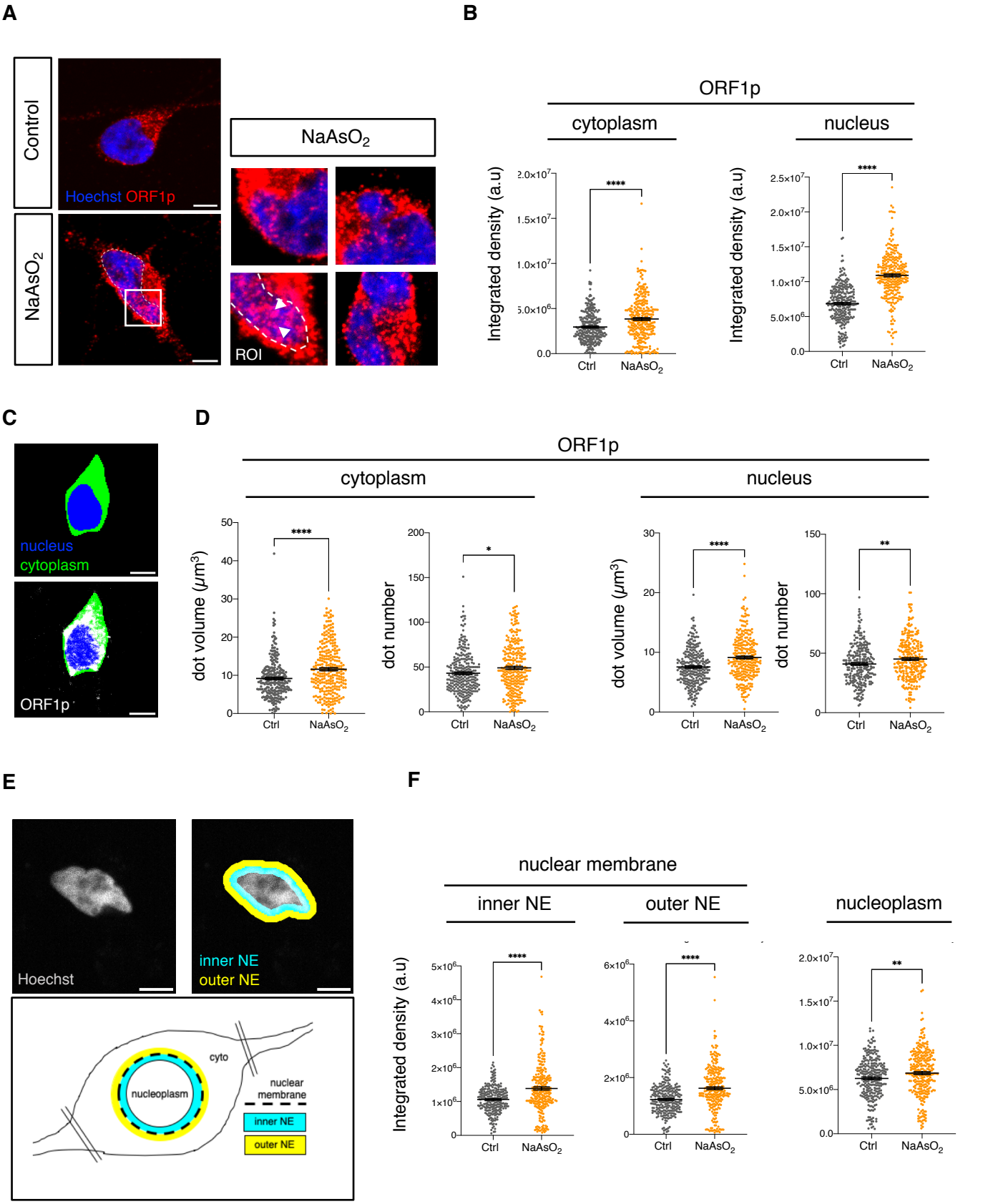
A
Control
NaAsO2
Hoechst ORF1p
NaAsO2
ROI
B
ORF1p
cytoplasm
nucleus
Integrated density (a.u)
Ctrl
NaAsO2
C
nucleus
cytoplasm
ORF1p
D
ORF1p
cytoplasm
nucleus
dot volume (μm3)
dot number
Ctrl
NaAsO2
E
Hoechst
inner NE
outer NE
cyto
nucleoplasm
nuclear membrane
inner NE
outer NE
F
nuclear membrane
inner NE
outer NE
nucleoplasm
Integrated density (a.u)
Ctrl
NaAsO2

Fig. 2

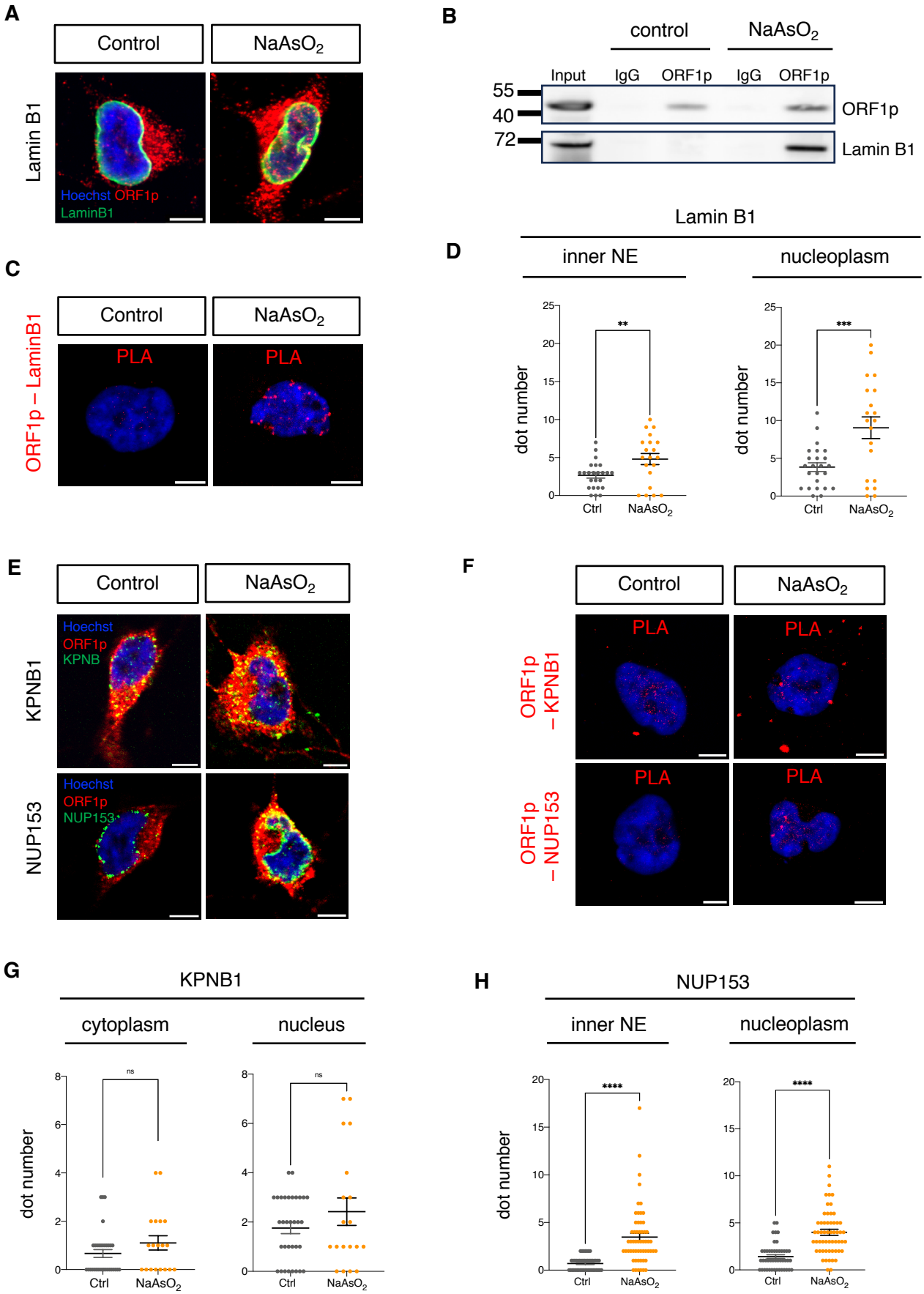
A
Control
NaAsO2
Lamin B1
Hoechst ORF1p
LaminB1
B
control
NaAsO2
Input
IgG
ORF1p
IgG
ORF1p
55
40
72
ORF1p
Lamin B1
C
Control
NaAsO2
ORF1p – LaminB1
PLA
PLA
D
Lamin B1
inner NE
nucleoplasm
dot number
Ctrl
NaAsO2
E
Control
NaAsO2
KPNB1
Hoechst
ORF1p
KPNB
NUP153
Hoechst
ORF1p
NUP153
F
Control
NaAsO2
ORF1p – KPNB1
ORF1p – NUP153
PLA
G
KPNB1
cytoplasm
nucleus
ns
dot number
Ctrl
NaAsO2
H
NUP153
inner NE
nucleoplasm
****
dot number
Ctrl
NaAsO2

Fig. 3

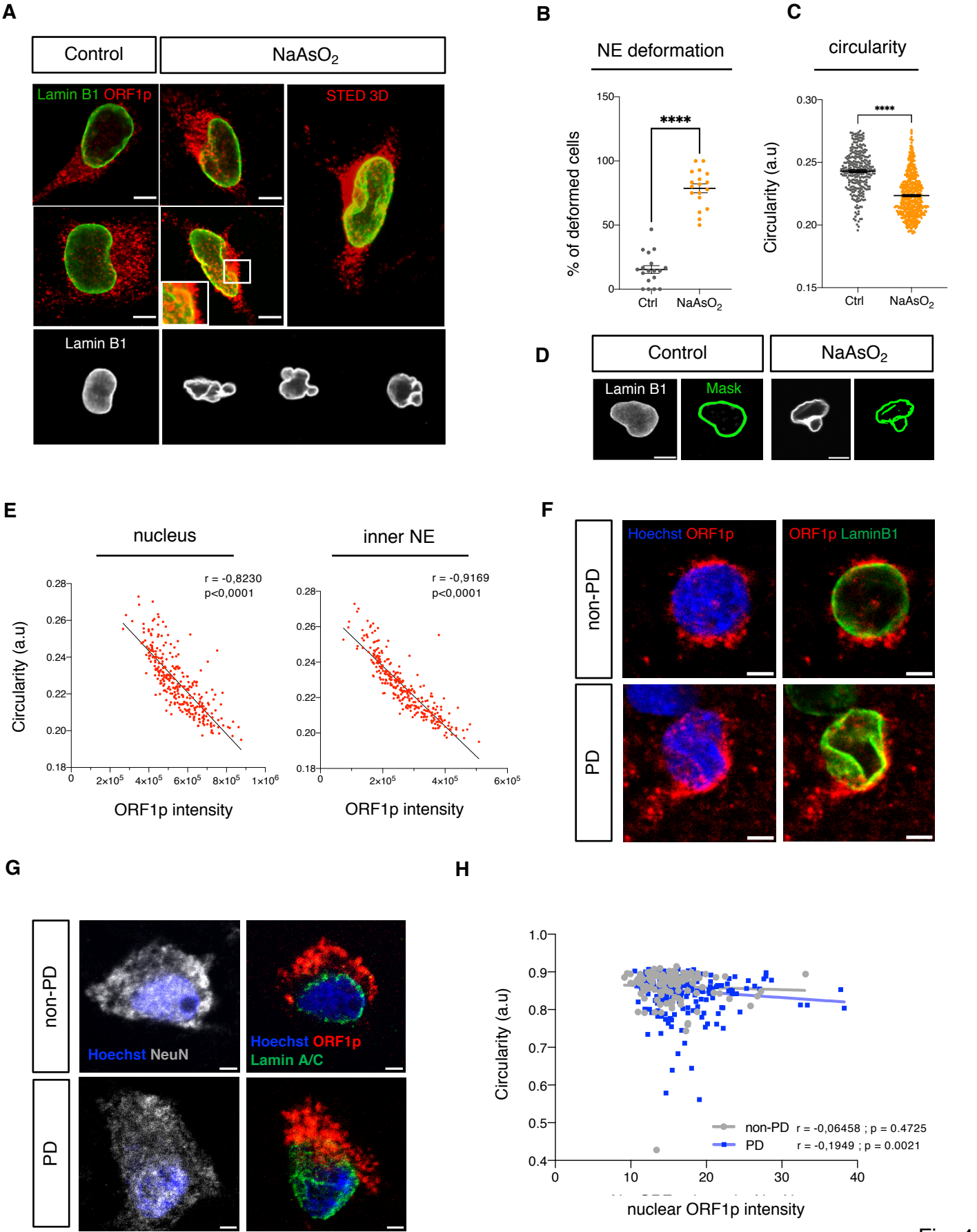
A
Control
NaAsO2
Lamin B1 ORF1p
STED 3D
Lamin B1
B
NE deformation
% of deformed cells
****
Ctrl
NaAsO2
C
circularity
Circularity (a.u)
****
Ctrl
NaAsO2
D
Control
NaAsO2
Lamin B1
Mask
E
nucleus
r = -0,8230
p<0,0001
Circularity (a.u)
ORF1p intensity
inner NE
r = -0,9169
p<0,0001
ORF1p intensity
F
non-PD
PD
Hoechst ORF1p
ORF1p LaminB1
G
non-PD
PD
Hoechst NeuN
Hoechst ORF1p
Lamin A/C
H
Circularity (a.u)
non-PD r = -0,06458 ; p = 0.4725
PD r = -0,1949 ; p = 0.0021
nuclear ORF1p intensity

Fig. 4

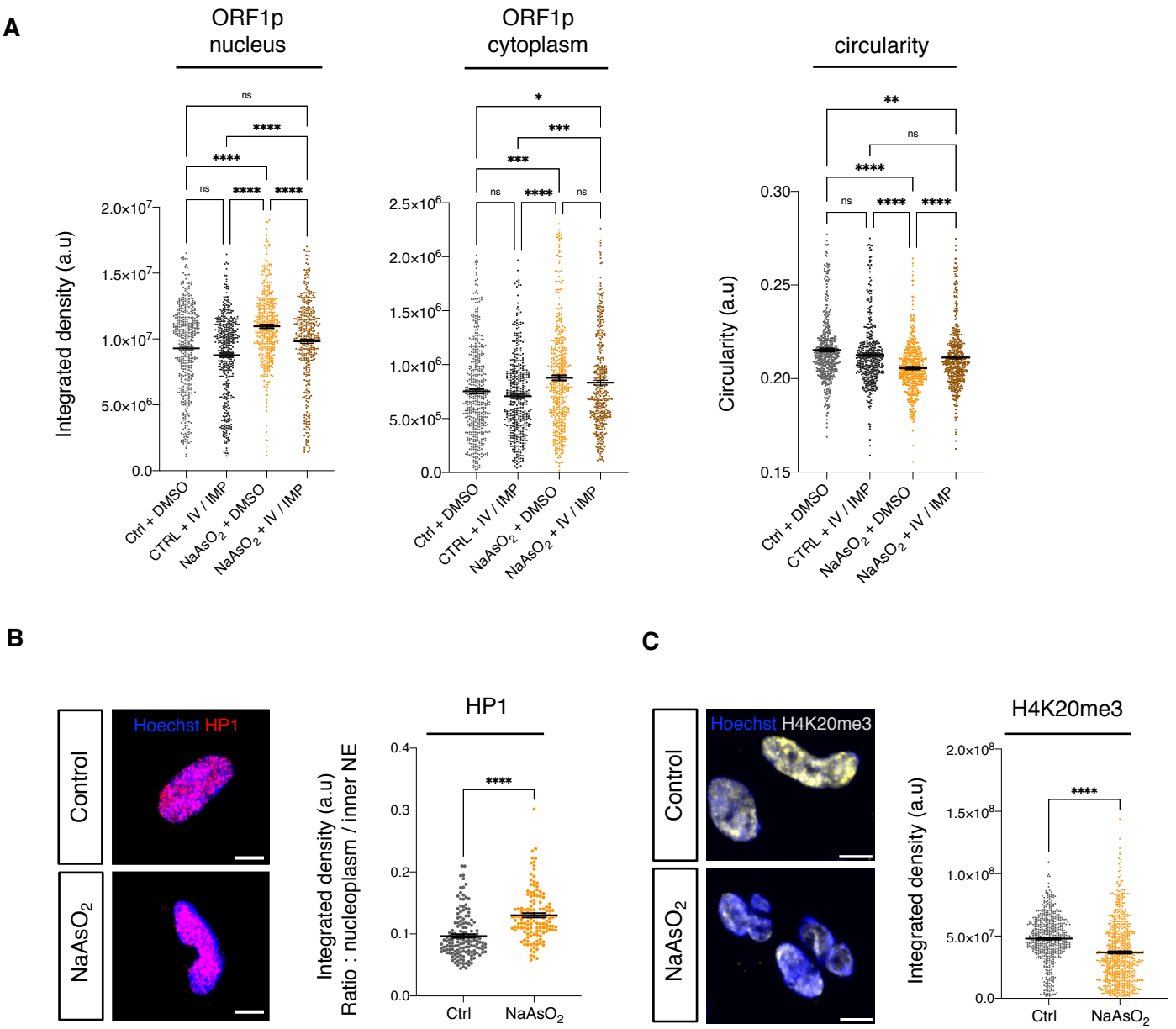
A
ORF1p nucleus
ORF1p cytoplasm
circularity
Integrated density (a.u)
Circularity (a.u)
ns
****
***
*
**
Ctrl + DMSO
CTRL + IV / IMP
NaAsO2 + DMSO
NaAsO2 + IV / IMP
B
Control
NaAsO2
Hoechst HP1
HP1
Integrated density (a.u)
Ratio : nucleoplasm / inner NE
Ctrl
NaAsO2
C
Hoechst H4K20me3
H4K20me3

Fig. 5

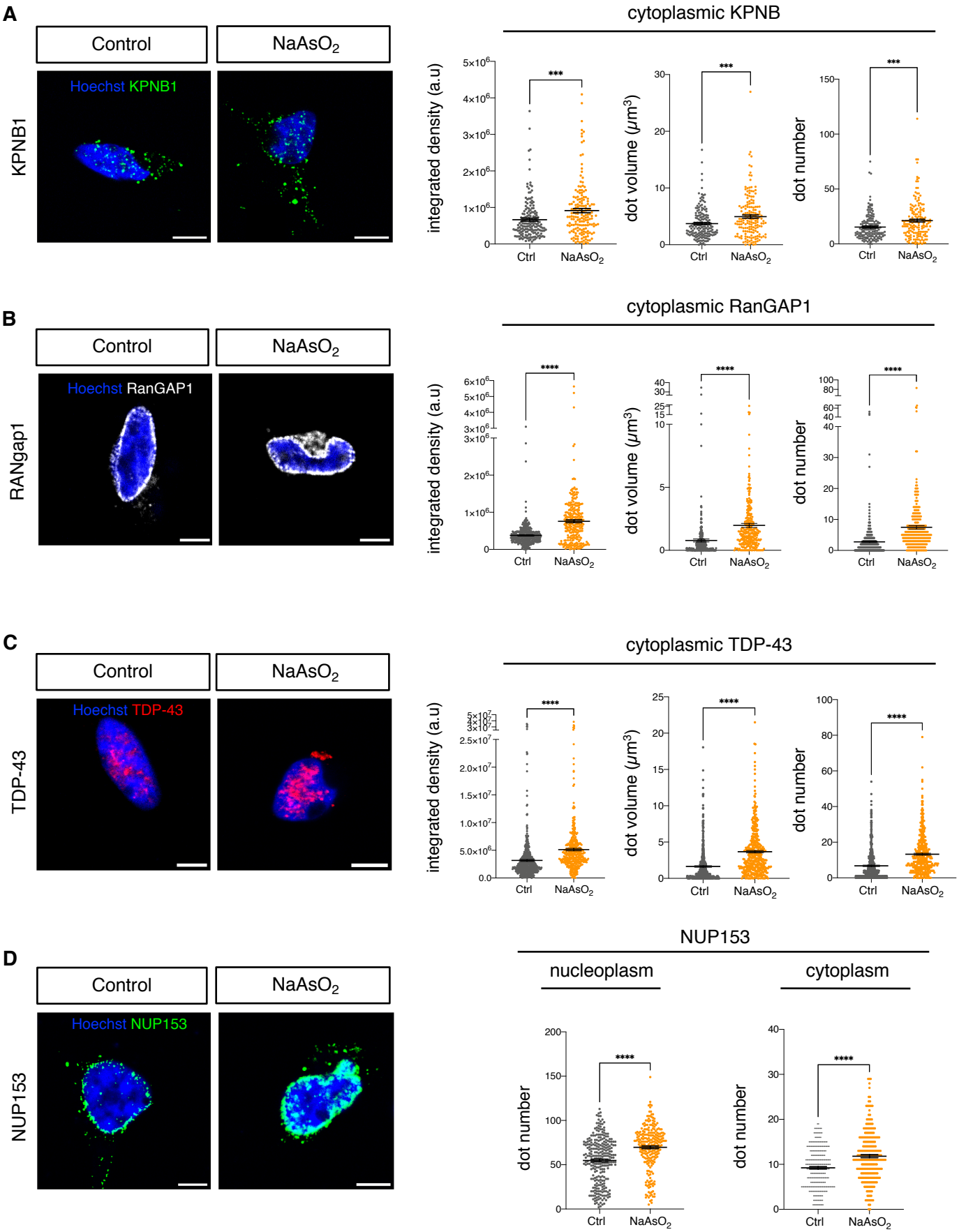
A
Control
NaAsO2
KPNB1
Hoechst KPNB1
cytoplasmic KPNB
integrated density (a.u)
dot volume (μm3)
dot number
Ctrl
NaAsO2
B
RANgap1
Hoechst RanGAP1
cytoplasmic RanGAP1
C
TDP-43
Hoechst TDP-43
cytoplasmic TDP-43
D
NUP153
Hoechst NUP153
nucleoplasm
cytoplasm

Fig. 6

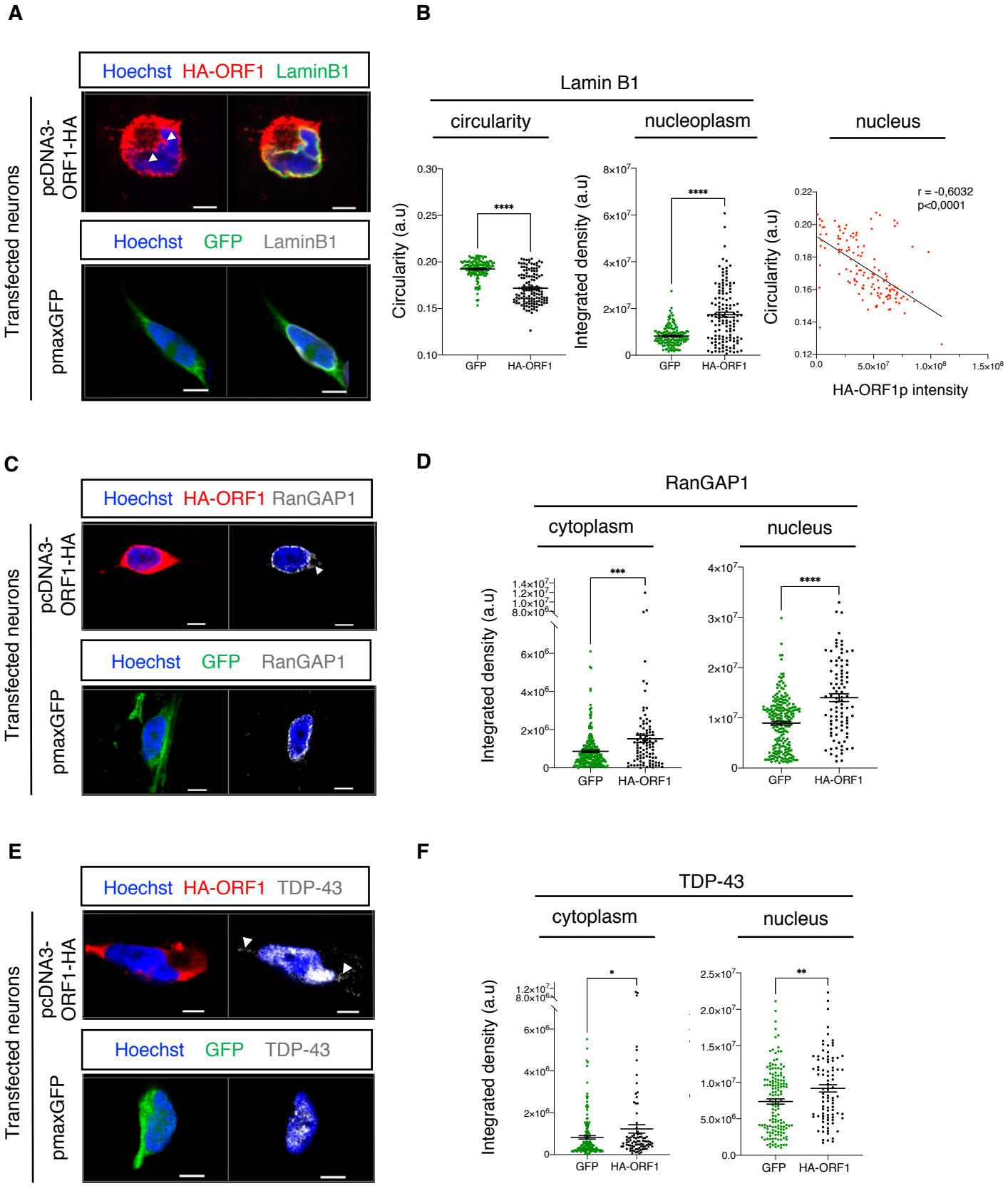
A
Hoechst HA-ORF1 LaminB1
Transfected neurons
pcDNA3-ORF1-HA
Hoechst GFP LaminB1
pmaxGFP
B
Lamin B1
circularity
nucleoplasm
nucleus
Circularity (a.u)
Integrated density (a.u)
****
GFP
HA-ORF1
r = -0,6032
p<0,0001
HA-ORF1p intensity
C
Hoechst HA-ORF1 RanGAP1
Hoechst GFP RanGAP1
D
RanGAP1
cytoplasm
nucleus
***
****
E
Hoechst HA-ORF1 TDP-43
Hoechst GFP TDP-43
F
TDP-43
cytoplasm
nucleus
*
**

Fig. 7

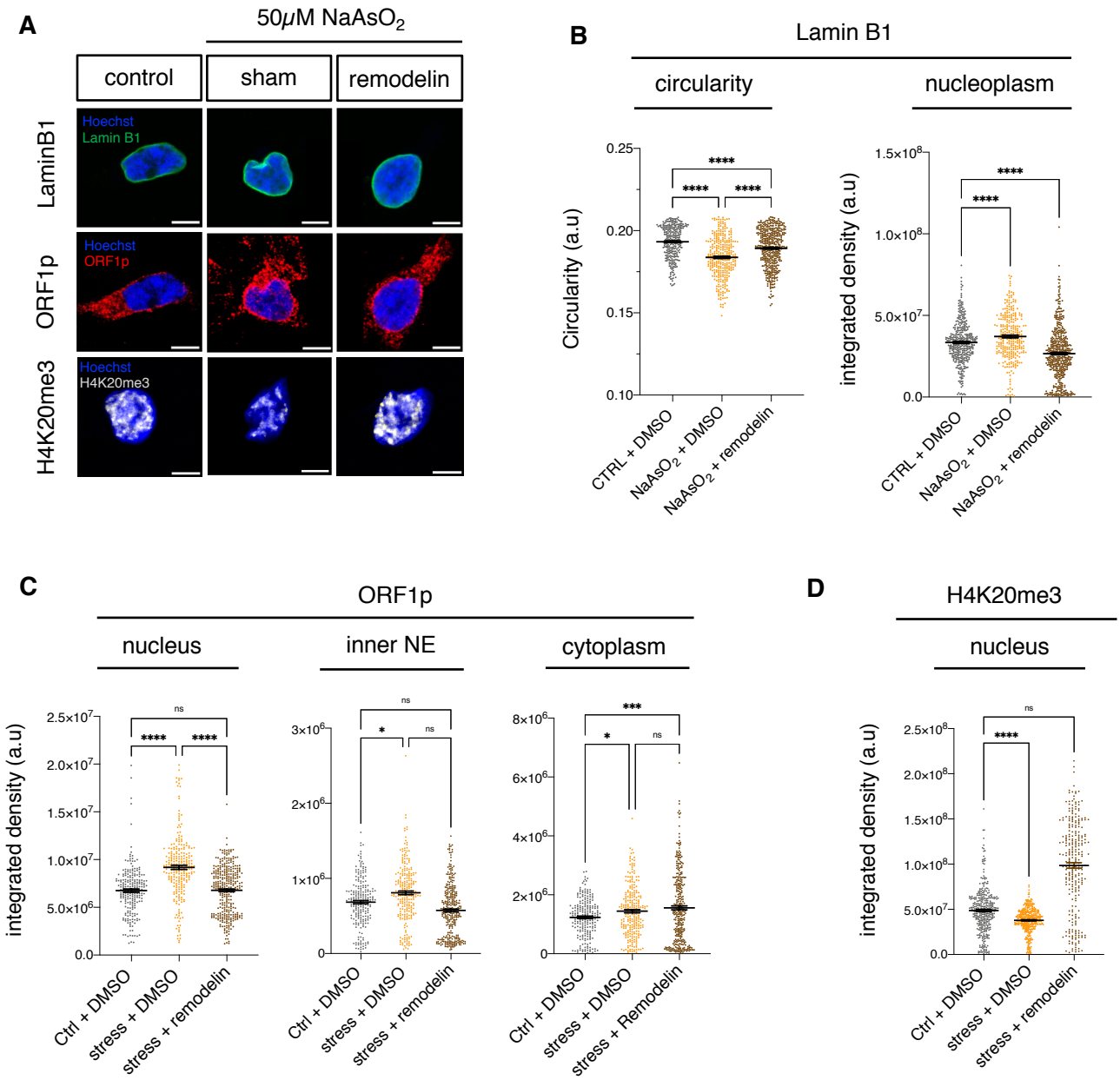
A
50μM NaAsO2
control
sham
remodelin
LaminB1
ORF1p
H4K20me3
Hoechst
Lamin B1
Hoechst
ORF1p
Hoechst
H4K20me3
B
Lamin B1
circularity
nucleoplasm
Circularity (a.u)
integrated density (a.u)
CTRL + DMSO
NaAsO2 + DMSO
NaAsO2 + remodelin
C
ORF1p
nucleus
inner NE
cytoplasm
integrated density (a.u)
Ctrl + DMSO
stress + DMSO
stress + remodelin
stress + Remodelin
D
H4K20me3
nucleus
integrated density (a.u)
Ctrl + DMSO
stress + DMSO
stress + remodelin

Fig. 8